CESR-X: In-Tunnel Conversion of CESR into Bright X-Ray Source

Ivan Bazarov, Yulin Li, Richard Talman,
Cornell Laboratory of Elementary-Particle Physics
Ken Finkelstein, Cornell High Energy Synchrotron Source
Lois Pollack, Cornell Department of Applied and Engineering Physics
Ken Soong, Cornell Physics Department

March 17, 2008

Contents

Abstract

A plan to convert CESR into a high brightness x-ray source is described. This conversion is compatible with, indeed needed for, the eventual high brightness, fast timing operation promised by the Energy Recovery Linac (ERL) project. Being relatively inexpensive, and relying on well-tested and conservative principles, this conversion can be completed in the near future. One role of this project will be to begin to perform many of the experiments that make the ERL project so exciting. Another role will be to drive the development (both hardware and personnel) for the unprecedented challenge of the x-ray beamlines needed to exploit the promised new capabilities. Though the achievable x-ray brightness is less than promised by a mature ERL, it will be at least three orders of magnitude higher than currently available at CHESS in at least ten beamlines and four orders of magnitude higher in three long undulator lines – for sub-Angstrom wavelengths their brightness will be higher than those of existing and planned rings. Similarly, with its flexible fill pattern, high charge per bunch capability, and millimeter-long bunch length capability, this ring will be more than competitive with existing facilities in real time, dynamical evolution studies. These studies will lead naturally into the faster timing studies that will be made possible by even shorter high energy linac pulses.

An option/upgrade with all 12 CESR-C wigglers installed to increase damping is also discussed briefly. As well as tripling the brilliance of the x-ray source, this would provide a prototype International Linear Collider (ILC) damping ring prototype quite close to what is really required for the ILC—namely less than 2 nm emittance at 5 GeV.

1 Introduction

1.1 Motivation, Schedule, and Parameters

With annual world-wide expenditures for new x-ray facilities being some billion dollars per year, there can be no doubt that there is great optimism concerning the future of this field of science. A strong physics case has been made for converting the Wilson laboratory into an x-ray source, now that the CLEO elementary particle project is winding down. This case has mainly been based on the ERL project, which promises "next generation" performance in both x-ray brightness and femtosecond timing capability. An aspect of this program that has not been well spelled out so far is the continuation and expansion of the CHESS program during the more than decade period until (optimistically) the ERL could begin operation.

This report describes a reconfiguration (called CESR-X here) of the CESR ring into a minimum emittance (and hence high brightness and high coherence) x-ray source – at $E_e = 5\,\mathrm{GeV}$ the emittance will be $\epsilon_x = 3.2\,\mathrm{nm}$, scaling as $1/E_e^2$. Since a ring with these properties is a required part of the eventual ERL facility, the main case to be made here is that this reconfiguration should commence at the earliest possible time.

There are two main reasons why this timely start is urgent. The first is that the same scientific case that has been made for new x-ray sources in general, and for the Cornell ERL in particular, provides motivation for getting started on the physics immediately. The ERL, once it delivers at promised performance levels, will enable certain experiments that could not soon be done, but there are far more experiments that are impractical at present, but will be possible with CESR-X. The second main reason is that development of the x-ray specific instrumentation needed for the new generation of experiments (and of the developers themselves) is at least as challenging as the proposed new accelerator developments. Experience has shown that such developments can only progress satisfactorily in true "battle conditions" with real beams and with intermediate term scientific goals steering toward ultimate goals.

One can evaluate next generation x-ray experiments in terms of their emphasis on soft (say less than 10 keV) or hard (greater than 10 keV)—for wavelengths this arbitrary boundary is at roughly one Angstrom. Light sources can also be differentiated upon whether they high "brightness" or "fast timing". It is pointless to try to order the importance of these attributes. Part of the reason for the proliferation of light sources is that all four categories of experiment are important.

For example, for inelastic scattering from materials, for which energy level separations are only a few electron volts, the appropriate x-ray energy resolution needed is easier to achieve with soft than with hard x-rays. Other examples would be photoemission-based techniques such as PEEM and ARPES, where the soft x-rays are a more natural choice.

Similarly, for surface physics, where even electron microscopy is practical, soft x-rays can be ideal. Soft x-rays are appropriate also for many small sample

chemistry applications. In spite of the large number of existing facilities where experiments like these are practical, the proposed NSLS-II project emphasizes this soft x-ray regime.

Continuing this crude survey, the significantly bright hard x-ray sources are at Argonne (APS), Grenoble (ESRF), and Japan (SPRING-8). For x-ray diffraction experiments, especially with large samples, high pressures, etc. the penetrating power of hard x-rays is essential. A typical example is a study of high pressure performance of carbon nanotubes by Wang and Zhao [1]. And hard x-rays are needed for the same reasons in coherent imaging, medical science, geology, and so on. By virtue of CESR's relatively high energy, CHESS has, for more than two decades, contributed importantly in these areas. CESR-X would enable Cornell to continue, or rather rejoin, its competition with these facilities.

The main requirements of the magnetic lattice of a hich brilliance light source are to be achromatic, with transverse dispersion minimized. These are the same as the requirements for the damping ring needed for a linear collider such as the International Linear Collider (ILC). As well as being a state of the art light source, the proposed project can also be regarded as a first-rate prototype (both as regards beam energy and emittances) for the ILC—a big step closer, for example, than the CESR-TA prototype, to what is actually needed.

It is important, also, for the lattice to be appropriate for its eventual application as part of the ERL. The requirement to be achromatic is satisfied and, because of its extremely small dispersion, the lattice is already as isochronous as possible, consistent with low cost and high modularity. Should precise isochronicity is required for the ERL, then some lattice reconfiguration will be required. Such studies have not yet been performed.

Table 1: CESR-X parameters. All entries assume 5 GeV operation, except the fifth column and parenthesized entries in the fourth column.

Parameter	Symbol	Unit	Baseline	Wiggler Option
beam energy	E_e	GeV	5.0(/4.0)	5.0/4.0
beam current	I_e	A	0.3	0.2
magnetic field	B	T	0.384	2.0
bend radius	ρ	m	43.44	8.34/6.67
cell bend length	L_b	m	6.498	
bend angle per cell		r	$2\pi/42$	
total bend length	$L_B = 42L_b$	m	272.9	5.2
radiation integral	$L_B B^2 E_e^2$	$\mathrm{m\,T^2\,GeV^2}$	1006/412	963/612
circumference	C	m	763.74	
horizontal tune	Q_x		38.90	
vertical tune	Q_y		20.68	
longitudinal tune	Q_z		0.009	
r.m.s. energy spread	σ_δ		0.00065	
r.m.s. bunch length	σ_{ct}	mm	2.9	
horizontal emittance	ϵ_x	nm	3.2	1.6/0.82
vertical emittance	ϵ_y	pm	32.	16/8.2
energy loss per turn	U_0	MeV	1.273(/0.52)	2.506/1.292
radiated power		MW	0.38	0.50/0.26
vert. damping lifetime	$1/\alpha_y$	turns	3928	1964/3845
number of RF cavities			2 or 3	4
max. horizontal beta	$\beta_{x,\mathrm{max.}}$	m	26.5	
max. horizontal beta	$\beta_{y,\mathrm{max.}}$	m	18.	
min. horizontal beta	$\beta_{x,\mathrm{min.}}$	m	1.1	
min. horizontal beta	$\beta_{y,\mathrm{min.}}$	m	3.1	
max. dispersion	$D_{\mathrm{max.}}$	m	0.2	
min. dispersion	$D_{\mathrm{min.}}$	m	0	
max. brilliance @10. keV	$\mathcal{B}_{\mathrm{max.}}$	$\frac{10^{20}\mathrm{photons}}{\mathrm{s\,mm^2\,mr^2\,0.1\%B.W.}}$	10.5	28/≈80

1.2 Performance as X-Ray Source

1.2.1 Brilliance

The brilliance expected for the **A** lines (12.3 m straights for insertion devices) of CESR-X are shown in Fig. 1, and compared with the performance of other rings. The brilliance of CESR-X is close to that of NSLS-II for soft x-rays, and well above both NSLS-II and APS from there up to about 50 keV. APS brilliance will be the highest above that energy. Of course, the CESR-X spectrum can be expanded to higher energies, such as 100 keV, by operating at a higher undulator harmonic or by increasing K, as in the CHESS wiggler case.

Fig. 1 refers to a "baseline" configuration in which there are no damping wigglers in the ring. By using the twelve damping wigglers from CESR-C the emittance can be reduced as shown in Table 1. Since the brilliances scale (inversely) as the square of the horizontal emittance, the brilliance could be increased substantially in this way. This alteration would have the subsidiary benefit of converting the ring into a realistic prototype for an ILC damping ring.

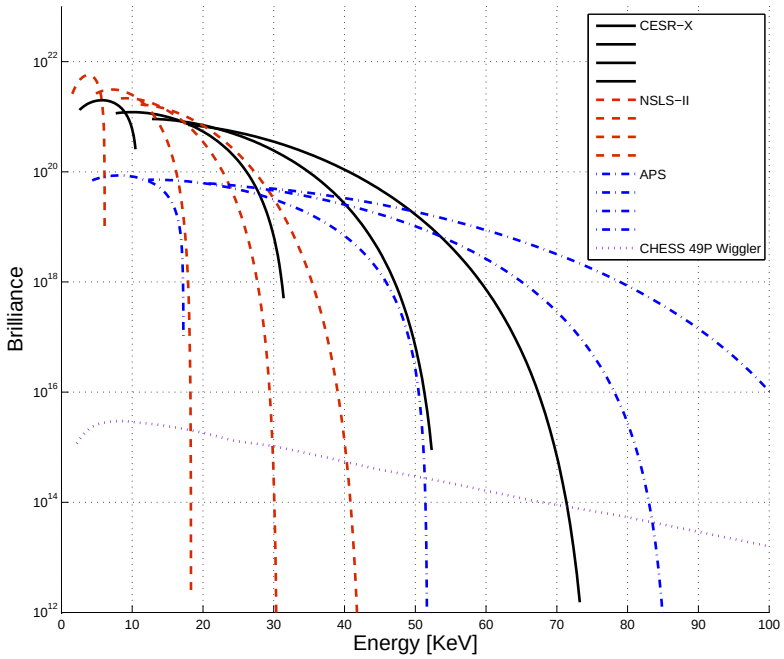

Figure 1: Brilliance curves for NSLS-II, CESR-X, and APS as calculated by SPECTRA8[2]. The brilliance units are conventional, photons/(s mm^2 mr^2 0.1%B.W.). In each case there is a sequence of undulator harmonics N=1,3,5,7. Electron beam energy E_e in GeV, and current I in mA, and undulator parameters, gap height g in mm, peak magnetic field B in T, period length λ_w in cm, total length L_w in m, and undulator parameter K, are, for NSLS-II: $E_e = 3$, $I = 500$, $g = 4$, $B = 1.682$, $\lambda_w = 1.4$, $L_w = 7.0$, $K = 2.2$, for CESR-X: $E_e = 5$, $I = 300$, $g = 7$, $B = 0.802$, $\lambda_w = 2.2$, $L_w = 12.3$, $K = 1.65$, for APS: $E_e = 7$, $I = 100$, $g = 20$, $B = 0.490$, $\lambda_w = 2.7$, $L_w = 2.4$, $K = 1.234$. The CHESS curve, from Shen[3], assumes 49-pole wiggler operation with CESR at 5.3 GeV and beam current 0.3 A. As mentioned in the text, and in Table 1, these brilliances could be further increased by (optionally) including damping wigglers in the ring.

The number of uses for x-rays is almost uncountably large, and the majority of them do not impose particularly stringent constraints on the source performance. As with all other rings, a substantial fraction of CESR-X experiments will be 'bread-and-butter' experiments that could be performed at other light sources. Enthusiasm for CESR-X is centered on the remaining, more fundamental experiments for which the facility is at or beyond the frontier of what is possible world wide. For CHESS this is not new. Because of CESR's relatively high energy and the correspondingly good flux of ultrashort wavelength photons, CHESS has traditionally been strong in this area. Unfortunately CHESS lost this position a few years ago. The present proposal can also be expressed as a plan to put CHESS back on the frontier.

Much of the content of Fig. 1 can be understood in simple terms. At the undulator location the distributions of transverse displacements of electrons and photons are identical. After monochromatization, the rms angular spread of the n'th forward undulator "spike" is given by

$$\sigma_{\gamma,\vartheta}^2 = \frac{1}{\pi}\,\frac{1+K^2/2}{\gamma^2}\,\frac{1}{N_w n} \tag{1}$$

where the standard CESR-X undulator will have about $N_w = 100$ periods (or a small multiple of 100). This can be compared to the horizontal angular spread of the circulating electrons, which satisfies

$$\sigma_{e,\theta}^2 = \frac{\epsilon_x}{\beta_x}. \tag{2}$$

Since the eventual x-ray angular distribution is a convolution of these two distributions, it is important for $\sigma_{e,\theta}$ to be at most comparable in magnitude to $\sigma_{\gamma,\vartheta}$.

Accepting $n = 1$, and using values from the caption to Fig. 1 and entries in Table 4, one gets that an emittance of about $\epsilon_x = 1\,\mathrm{nm}$ would be required to render negligible the contribution of the electron distribution to the photon angular distribution.

For CESR-X the horizontal emittance will be $\epsilon_x = 3.2\,\mathrm{nm}$ and the vertical emittance will be negligibly small in the present context. The angular electron spread will therefore reduce the peak flux density by roughly a factor of three compared to the ideal scenario.

1.2.2 Coherence

Another fundamental assessment can be based on beam coherence – a challenge for modern x-ray physics. It took two centuries (following Young's two slit and Lloyd's mirror experiment) for the phenomenon to be further exploited in optical instruments, even though the wave nature of visible light had been demonstrated. It is now approaching one century since the Lloyd mirror experiment was first performed with x-rays.[4] In the meantime, because of the happy coincidence of atomic spacings with x-ray wavelengths, interference has

been of fundamental importance. But the dimensions of man-made structures have, until recently, been too coarse to make x-ray interferometry practical.

With recent advances in nanofabrication, and other instrumentation improvements, one can now strive to exploit x-ray interference as an active, rather than a passive tool. Only one of the impediments is relevant for this report. Will coherence of the CESR-X beam be high enough that the beam quality will not, all by itself, prevent successful interferometric measurements? A rough estimate follows.

From Eq. (2) one sees that the contribution of the electron beam to the angular spread can be made negligible by increasing β_x. But, for most purposes, this improvement would be spurious since the source width would be increased proportionally, which would reduce the transverse coherence proportionally.

The issue of coherence preservation depends strongly on the x-ray wavelength of interest. Reflecting the loss of coherence with increasing photon energy, one can define a "diffraction-limited transition wavelength"[5],

$$\lambda_{\rm dl} = \pi\epsilon_x, \tag{3}$$

above which the radiation is fully coherent and below which it is only partially coherent. Again the vertical emittance of CESR-X will be small enough to not impair the coherence for any x-ray energies of interest. But the value of ϵ_x for CESR-X will cause the coherence to fall off for photon energies exceeding 0.1 keV.

Als-Nielsen and McMorrow[6] show that the transverse coherence length at distance R from the source is given by

$$L_T \approx \lambda \frac{R}{4\sqrt{\epsilon_x \beta_x}}. \tag{4}$$

For 10 keV photons at CESR-X, this produces a horizontal coherence length of about 20 micrometers at $R = 100$ m. This is amply large for many samples of interest. The ten times larger vertical coherence length, along with horizontal collimation, will allow high coherence for 10 keV photons even though L_T is small compared to the undulator spike width at the same distance. Combining Eqs. (2) and (4), one finds that L_T, as a fraction of the spot size, is

$$\frac{L_T}{R\sigma_\vartheta} \approx \frac{\lambda}{4\epsilon_x}. \tag{5}$$

This fraction gives the degree of collimation (or sample size compared to beam size) required to illuminate a sample with radiation that can be regarded as highly coherent. This formula can be seen to contain the same physics as Eq. (3). By being independent of β_x, it shows that one cannot enhance the coherent fraction by adjusting the accelerator optics at the undulator location. For CESR-X, obtaining full coherence at 10 keV will entail collimation that causes roughly two orders of magnitude loss of flux.

This calculation, all by itself, shows that the beams currently available at CHESS, with emittances some fifty times higher than CESR-X, cannot realistically be competitive for experiments that rely on transverse beam coherence.

Als-Nielsen and McMorrow[6] show that the longitudinal coherence length is given by

$$L_L = \frac{\lambda}{2\Delta\lambda/\lambda}, \tag{6}$$

Since $\Delta\lambda/\lambda$ is controllable by monochromatization, this length is somewhat adjustable, though typically $L_L << L_T$. Nevertheless, it should be practical to produce longitudinal coherence length exceeding one micrometer at 10 keV. The possibility of x-ray interferometry is one of the frontier challenges CESR-X is intended to attack. Though very hard, it will be necessary (to produce interference), and presumably possible, to adjust the length difference between split beamlines to be less than L_L. Incidentally, the electron energy spread in CESR-X will be small enough to be negligible in this context.

1.2.3 Timing

An exciting new, but still largely unexplored area concerns the observation, using x-rays, of system evolutions on femtosecond time scales. By virtue of their extremely high peak brilliance and correspondingly short pulse lengths, the FEL's, if their fundamental problems (especially their erratic beam properties), will dominate this field. This is especially true for soft x-ray experiments in which target destruction is inevitable.

For dynamic evolution experiments demanding hard photons, high frequency (GHz) repetition rates and ultrashort, femtosecond, time resolution, the Cornell ERL will be unsurpassed.

For some processes it is evolution on far slower than femtosecond time scales that is of interest. A study of transient structural changes in organic samples by Techart et al., using 16.5 keV x-rays is an example [7] on picosecond time scales. Experiments like these typically require dedicated storage ring reconfiguration which is inconvenient for most other users. Furthermore, the number of facilities where such experiments can be performed is small. With its bunch pattern flexibility, millimeter length bunches, and high charge per bunch capability, CESR-X will be uniquely suitable for experiments like these. Charge density wave investigations, as proposed by Joel Brock [8], using the natural MHz scale repetition rate of CESR-X, either with adjacent buckets filled, or with a few intense bunches in the ring, will also be practical.

Dynamical evolution of biological and other material processes on even longer – millisecond, microsecond, nanosecond – time scales are also of interest. Many of these are subject to in-situ characterization, an area in which CHESS has considerable experience. Some of these applications are discussed in a later section. Though experiments like this can be done at numerous laboratories, many require special set ups and quite high x-ray energies. The list of appropriate sources is therefore quite short. Furthermore, even on that short list, objections from other users tend to restrict availability of bunch patterns that have been optimized for timing applications.

2 Lattice Properties

This report updates and expands upon earlier reports [9][10][11][12]. Minimizing beam emittance places heavy demands on the lattice Twiss functions and dispersions. Fortunately these demands are either consistent with improved x-ray beamline performance (as in the case of low emittance) or at least neutral (as in the case of choice of Twiss-β-functions). The emphasis in the accelerator design strategy has been on robust and modular approach to the ring lattice in addition to ensuring the ability to reuse as much of the existing infrastructure in Wilson tunnel as practically possible [11, 12].

2.1 Design Strategy

To obtain brilliant x-ray beams it is essential (especially for the horizontal plane) for transverse emittances to be minimized. This requires both Twiss function β_x and dispersion function $D(s)$ to be very small, with both passing through minima at s=0, the centers of the bending magnets. To obtain the theoretical minimum emittance, $D(0)$ would be close to, but not exactly equal to zero at these points. It greatly simplifies the modularity of the lattice to adjust $D(0)$ exactly to zero at these points.

Then the *maximum* value of $D(s)$ will be an order of magnitude less in CESR-X than is typical, at present, in CESR. Also the optical functions everywhere in CESR-X will be almost as sensitive as in the intersection region of CESR. This will make the tuning of the machine more delicate than has been required for CESR.

For this reason it seems prudent to make the lattice as modular as possible. In spite of the requirement that CESR-X coincide (plus or minus some tens of centimeters) with the footprint of the present CESR storage ring, it has been possible to build the entire ring from just two "LEGO blocks". These are illustrated in Fig. 2. All length parameters for the ring are contained in this figure.

There is little or no arbitrariness in the proposed configuration. It is constrained by the geometry of the Wilson Lab tunnel, which is formed from six identical sextants, separated south (L0 in Wilson Lab nomenclature) and north (L3) by "long" **A**-straights, and southeast, northeast, northwest, and southwest (L1, L2, L4, L5) by medium length **B**-straights. This, plus the desire to minimize the emittance consistent with using magnets more or less like those presently in CESR, all but determines the complete design. Issues like this are discussed in greater detail in an earlier note [9].

In the proposed design there are, altogether, 42 of the bend cells, and 14 of the FODO cells. The FODO cells are grouped into two long **A**-straights with three FODO cells each (at locations L0, and L3) and four medium length **B**-straights with two FODO cells each (at locations L1, L2, L4, and L5). All other drift sections (which appear in quad-separated pairs in the bend cells) will be referred to as **C**-straights.

The lattice function boundary values will be the same at all boundaries: namely, $\beta_x = 1.0\,\mathrm{m}$, $\beta_y = 11.0\,\mathrm{m}$, $\alpha_x = \alpha_y = 0$, and $D = D' = 0$. Tuning the entire ring will therefore start by perfecting the tuneup of individual bend cells or, in the case of straight sections, with FODO sections consisting of a few basic cells. Then the same procedures will be applied mechanically to all the rest of the basic cells in the lattice. With this modularity, *all* lattice function variation can be exhibited in the three parts of Fig. 3. These patterns are repeated to fill the whole ring, as shown in Fig. 4.

Since the purpose of CESR-X is to produce x-rays, it is important to assess the number of lines and their properties. Many of the potential lines point more-or-less toward the existing Wilson laboratory building. These will be referred to as "easily accessible". The available straight section can be inferred from Fig. 2 and Fig. 3 and the total number and total lengths of straight sections from Fig. 4. Using the nomenclature defined previously, the straight sections are designated as being of types **A**, **B**, and **C**, as shown in Fig. 18. The two **A** lines, one north, one south, are made up of three FODO cells, meaning six drift regions, each of length 2.053 m, and a total free length of 12.3 m. Undulator design appropriate for these straights (and the others) is contained in Section 6.1, and in Table 4.

2.2 SRF Cryomodules

The most significant change in the present design (compared to reference [9]) was forced on us by RF requirements. We had assumed that the natural locations for RF cavities would be at one or more of the L1, L2, L3, or L4 straight section locations. Conversations with Sergey Belomestnykh disabused us of this notion. Availability of liquid helium was the main concern, and there is a strong motivation for leaving the RF cryomodules close to their present locations in the west flare. But the straight sections there were too short to accept the cryomodules.

This required a redesign, which amounted to reducing the **A** and **B** straights and lengthening all the **C** straights. Fortunately this proved possible, though it required redesign (stronger combined function focusing) of the bending magnets (described previously in reference [12] and repeated here in Section 4.1).

The newly-positioned cryomodules are shown in Fig. 9. To make a bit more room, the sextupoles have been removed from this cell. This particular bend cell is at an as-yet-undetermined location in the west flare, close to the present cryomodule location. No exact location has yet been proposed because of not-yet-understood interference with x-ray beamline positions. It needs to be investigated whether the number of cavities will need to be increased from two to three.

2.3 Beam Transfer From the Synchrotron to CESR-X

Another significant change from our earlier design [9] concerned injection into CESR-X. Conversation with Dave Rice impressed upon us the need for situating the pulsed CESR-X injection septum at a point in the lattice where β_x is large.

It was considered desirable to leave the synchrotron extraction hardware completely unchanged, which meant leaving the transfer location in the vicinity of L4. The prelimary L4 straight was too short to permit substantial increase in β_x. By canibalizing one bend cell on each side L4 it was possible to increase β_x, but only to 16 m, and at the cost of a β_y maximum exceeding 100 m. By canibalizing more of the ring a superior scheme could undoubtedly be worked out, but the further reduction in modularity made also this solution unattractive.

Fortunately there was a superior alternative. Reference to Fig. 3 shows that there is a significantly large β_x value in the regular bend cells. There are two such locations in each of the 42 bend cells in the ring. At those points $\beta_x = 26$ m, which is roughly the value in current CESR operation. By treating the $q1$ quad (at the center of the bend cell) as the final (off-axis) quadrupole in the transfer line, the pulsed septum can be located 12 meters into the standard bend cell. This is illustrated in detail in Fig. 5. The optical functions are shown in Fig. 6.

The proposed transfer line is considerably longer than the present synchrotron-to-CESR west transfer line. By redoing the synchrotron extraction scheme the line could be made somewhat shorter. But one new requirement of the line (compared to current CESR operation) is the "impedance match" from quite high beta functions in the synchrotron to low values in CESR-X. Achieving a great reduction of the length of line compared to that shown in Fig. 5 therefore seems unpromising. Tunnel conjestion through this area will therefore be serious. It can be seen from the figure that the quad locations have been synchronized with CESR-X magnet locations. This will permit the transfer line to be tucked up against CESR-X.

Should this congestion be judged to be unacceptable some alternative would have to be adopted. One alternative would be to move the injections to the L3 straight section in the north area, where there is more room. This would, however, sacrifice one of the high brilliance lines. Another option would be to perform the conventional construction needed to open up the L4 region.

2.4 Nudging the CESR-X Lattice onto the CESR Footprint

As the design stands, the lattice will match the Wilson ring within ± 0.40m. Initially, our hope was to reduce this deviation to the order of a few centimeters. To approach this, we allowed individual bending magnets to vary up to 15% in strength (though hoping for much smaller pertubation than this) while still preserving the symmetry of the lattice. Such bend variations have negligible effect on the betatron functions, but they do distort the dispersion function. This variation in field strength can easily be achieved by shimming the crowns appropriately. By varying the field strength of the magnets, we allow ourselves to adjust the bend angle contributed by each magnet and thus the overall shape of the beam's path. Of course, to preserve the 360° total bend requirement, any change in the bend angle of one magnet must be balanced by an equal and opposite change to another magnet.

To begin the beam path-correction procedure, we created a very simple (completely artificial) MAD lattice file, comprised of six 60° circular arcs, separated by straight sections. This lattice file represents the actual Wilson tunnel and MAD's survey data from this file was the reference path used when calculating the beam path's deviation. A Matlab script was created to take the survey output from MAD and create a list of angles and radii for both the reference and the beam path. The radii of the two paths at each respective angle were then compared and plotted as shown in Fig. 7.

We decided that a brute force approach, which minimized the sum of the squared error, was the simplest solution to our problem. With the brute force method, in order to obtain a solution in a reasonable amount of time, it was necessary to reconstruct some of the previously used procedures and methods. In the previous state, calling the MAD program to produce the survey output and reconstructing the data in a useable form required approximately 30 seconds per iteration. By developing a Matlab script to replicate the survey function of MAD, we were able to completely bypass the calling of MAD and reduce the previous 30 second run time to about 1 second.

In our brute force script we begin with an initial "measure of goodness" equal to the value of the sum of the squared difference between the radii of the beam path and the reference path for the entire lattice. The script begins its iterative process by randomly choosing one of the 21 unique magnets (M1) (in half the ring) and varies the magnet by a small amount δ. Afterwards, it randomly chooses one of the remaining 20 magnets (M2) and applies the opposite change. If the measure of goodness is lower than the previous lowest measure of goodness then the values for the magnets corresponding to M1 and M2 are saved and the process is repeated. However, if the measure of goodness does not decrease with our first choice of M2, then a different M2 is chosen until either the measure of goodness decreases or until all the magnets have been tried. In either case, a new M1 is chosen and the process is repeated. This entire process is repeated until no combination of changes to M1 and M2 is found to decrease the measure of goodness, in which case δ is reduced to the value δ_0/n, where δ_0 is the initial value for δ and n is the number of times δ has been defined. Once δ has been changed, the iterative process is again repeated. In this script, the user must define two constraints: the maximum change a magnet can undergo, in our case 15%, and the number of times δ can be decreased.

After a complete run of our brute force optimizer, we found that we could match the beam path and the reference path fairly well. With the constraint that the magnet strengths could not deviate more than 15%, we were able to reduce the original deviation from $\pm$0.40m to $\pm$0.15m, see Fig. 8. These changes had negligible effect on the Twiss betatron functions for the lattice. They perturbed the dispersion noticeably, but not enough to increase the horizontal emittance very much. One assumes, furthermore, that the ideal dispersion shape can be recovered by trimming the quadrupole currents. Neevertheless, since deviations from the footprint larger than $\pm$0.15m are probably acceptable, especially in the north and in the south, it will be appropriate to make further iterations, in order to further reduce the magnetic field trimming.

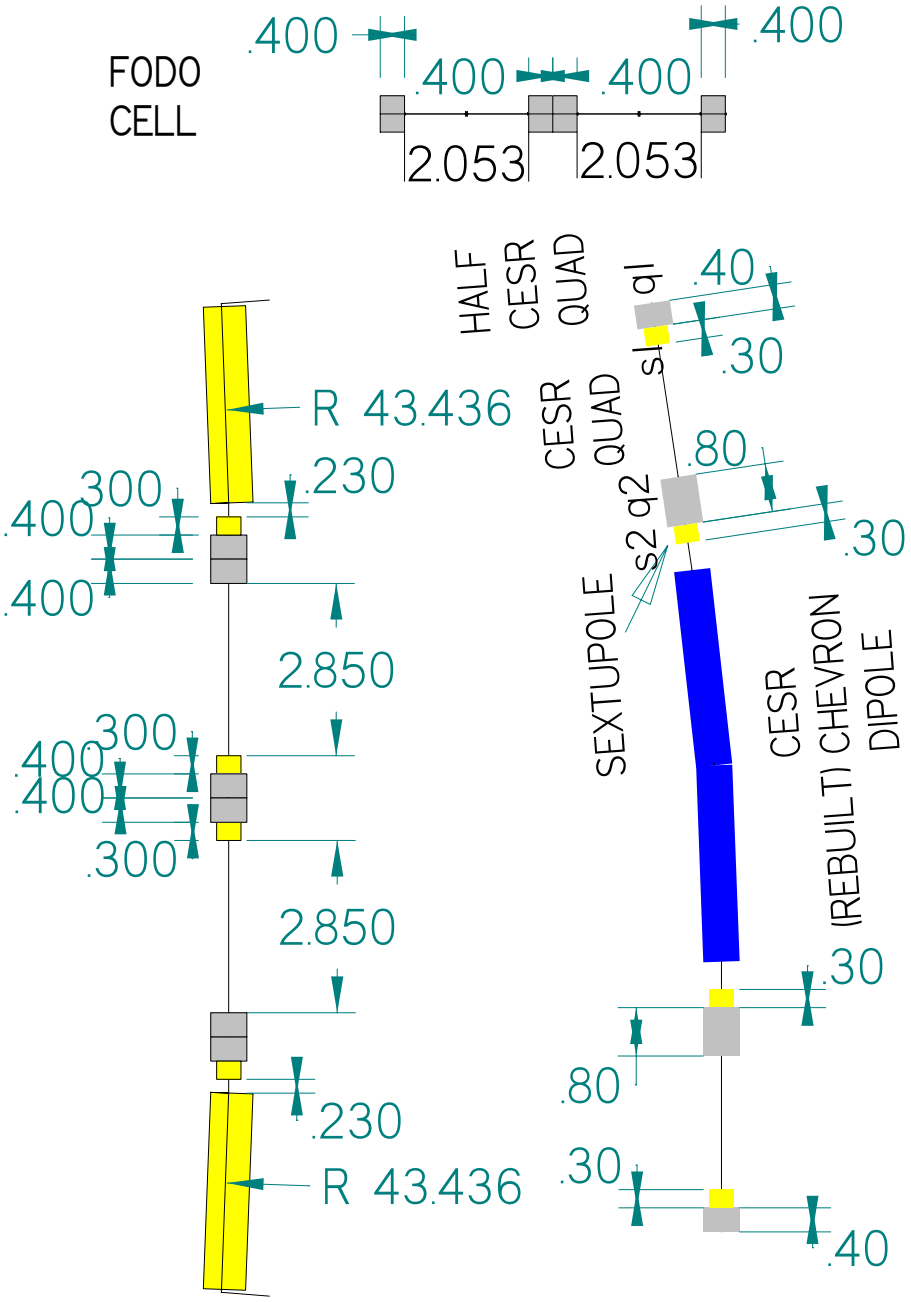

Figure 2: Cell detail. Straight sections are built from FODO cells shown at the top. A bend cell can be regarded as beginning at the bend center or with the bend at the cell center. This requires half magnets (length=3.498 m) at sector ends. Both cases are shown here.

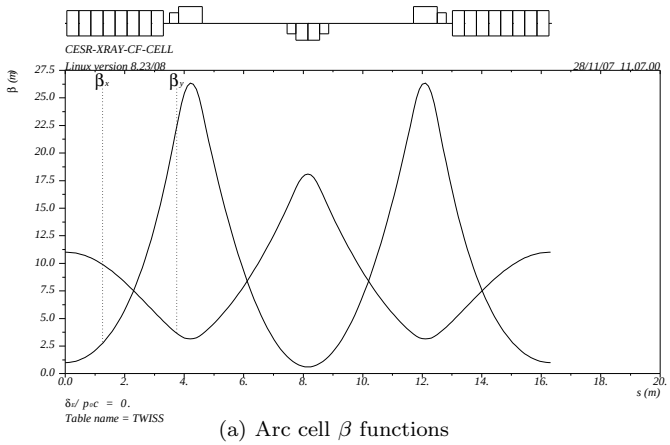

(a) Arc cell β functions

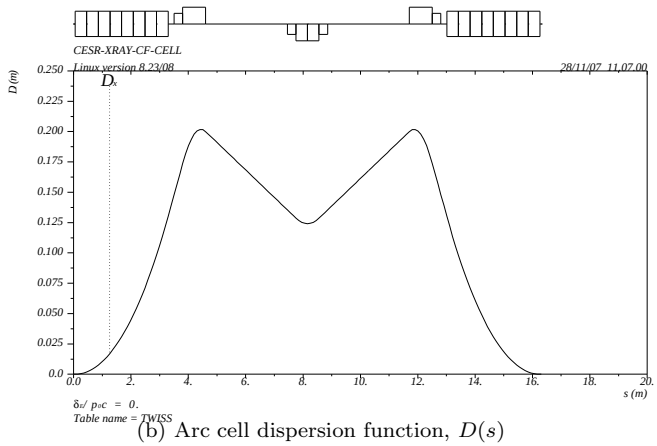

(b) Arc cell dispersion function, $D(s)$

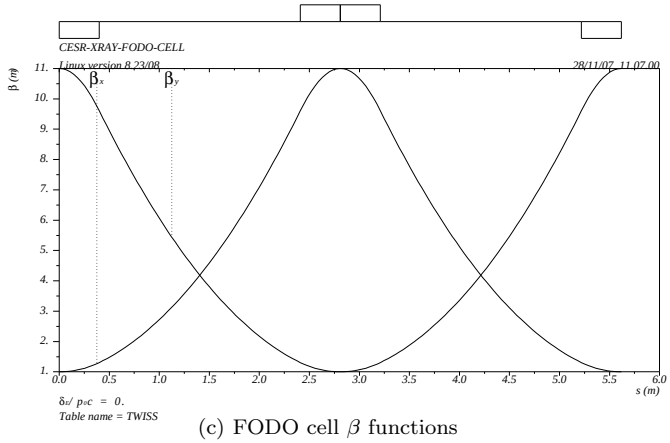

(c) FODO cell β functions

Figure 3: Optical functions of regular bend cell and of FODO straight cell. The CESR-X lattice is built entirely from these "LEGO blocks".[27]

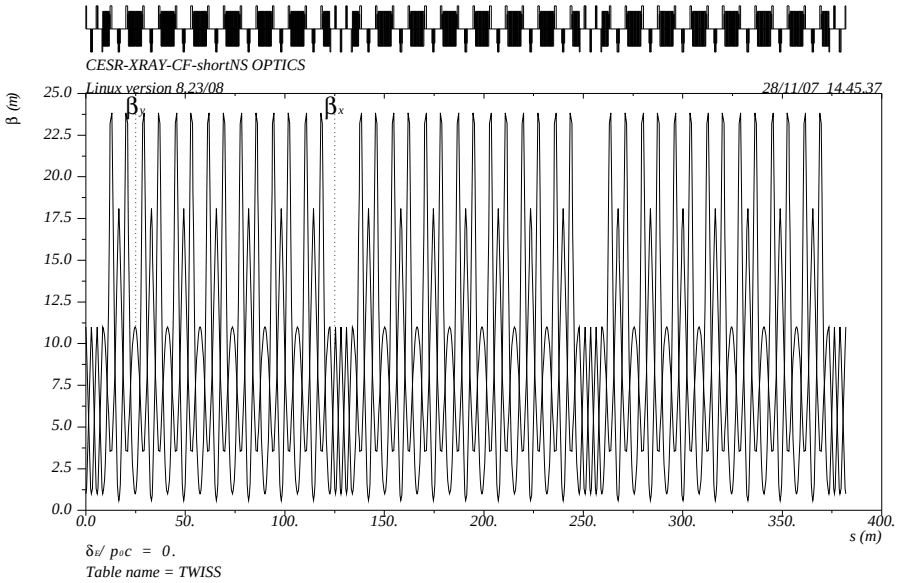

(a) β functions

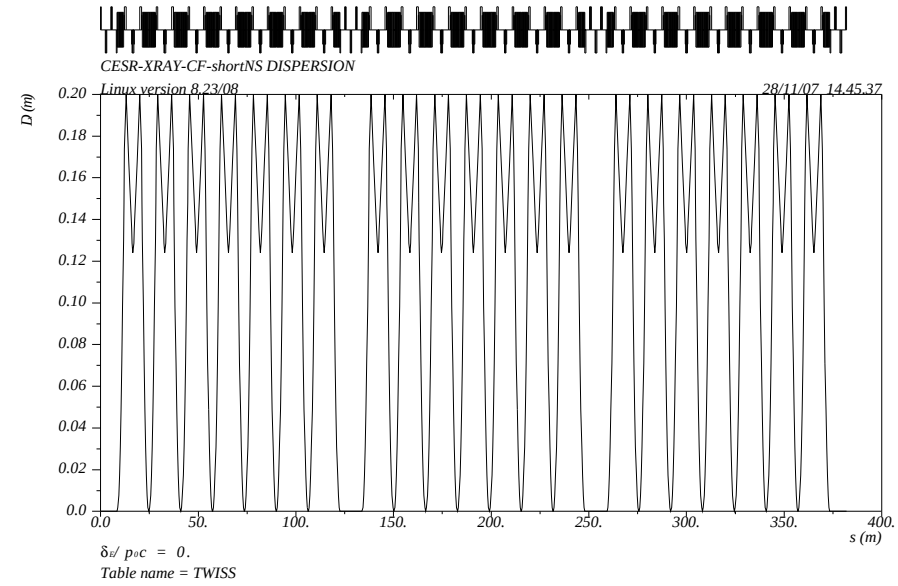

(b) Dispersion function, $D(s)$

Figure 4: Optical functions for half the ring, which has north-south and east-west mirror symmetry as well as order-reversal symmetry.

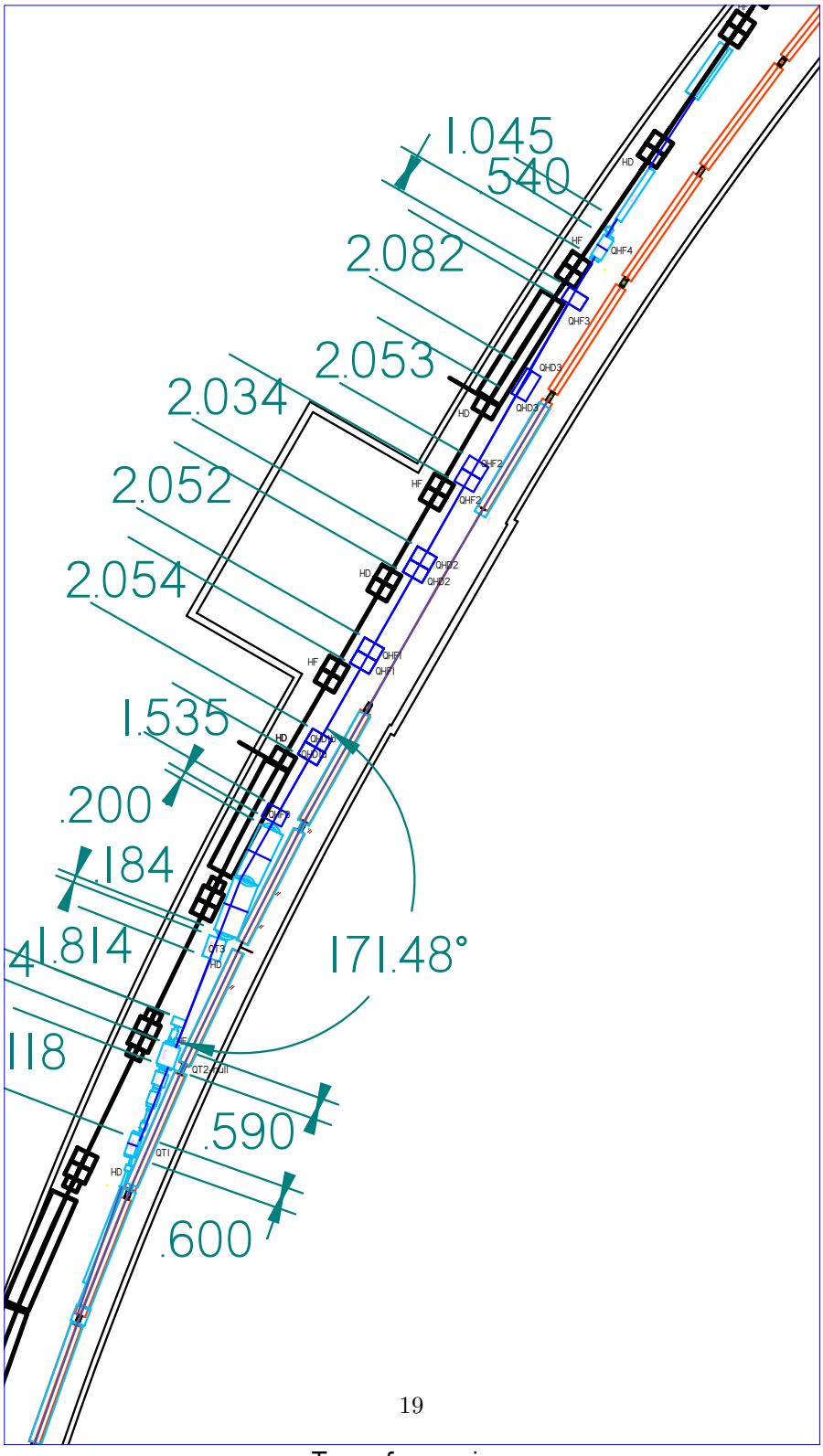

Figure 5: Transfer line layout, assuming extraction from the synchrotron is unchanged from its present configuration.

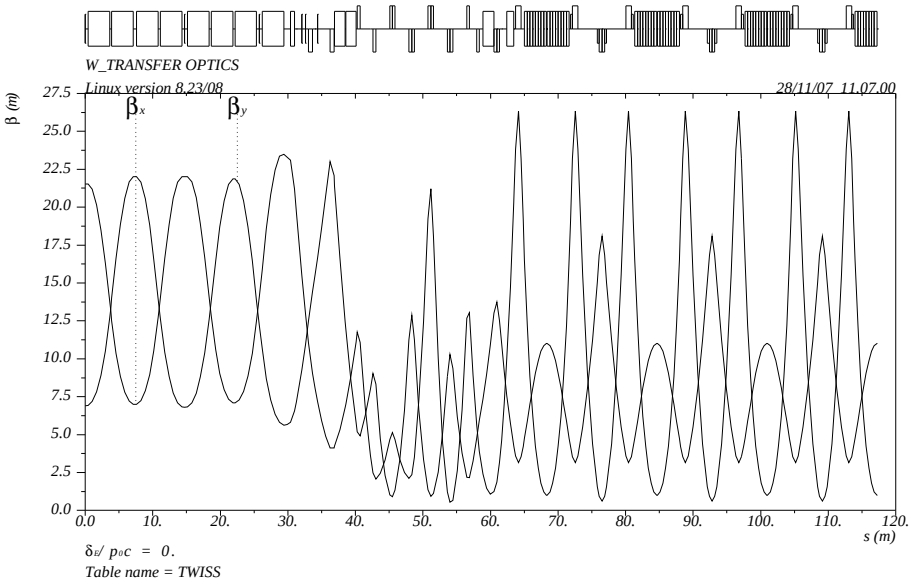

(a) β functions

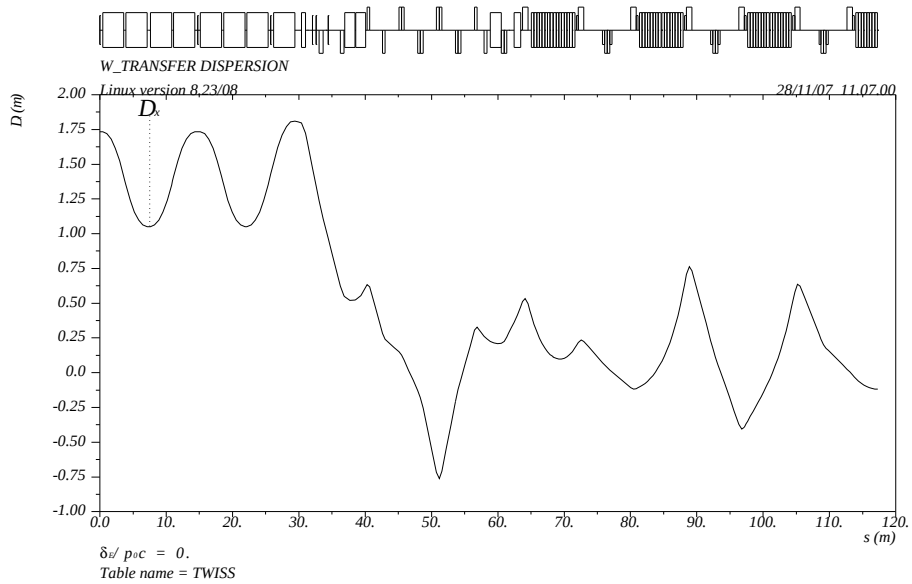

(b) Dispersion function, $D(s)$

Figure 6: Optical functions along injection transfer line. Precision geometry has not yet been worked out and the initial conditions in the synchrotron are not very well known. The match to dispersion in CESR-X is only fair, but the residual dispersion is comparable with the regular CESR-X dispersion.

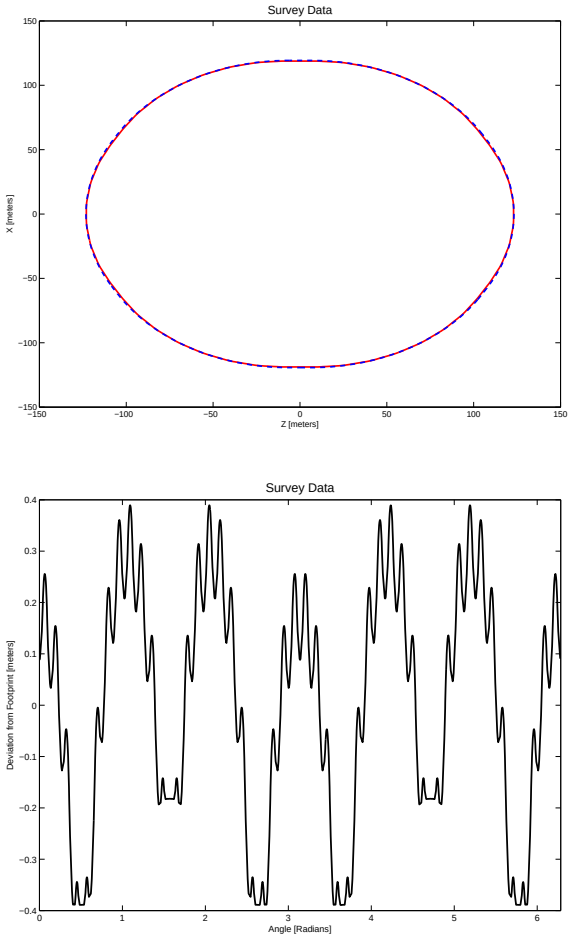

Figure 7: The top figure shows a plot of the survey data of the CESR-X lattice (in red) superimposed on the survey data of Wilson tunnel (in dotted blue). The differences in path radii are plotted as points on the bottom figure. We can see that the discrepancy has a span of about 0.8 meters.

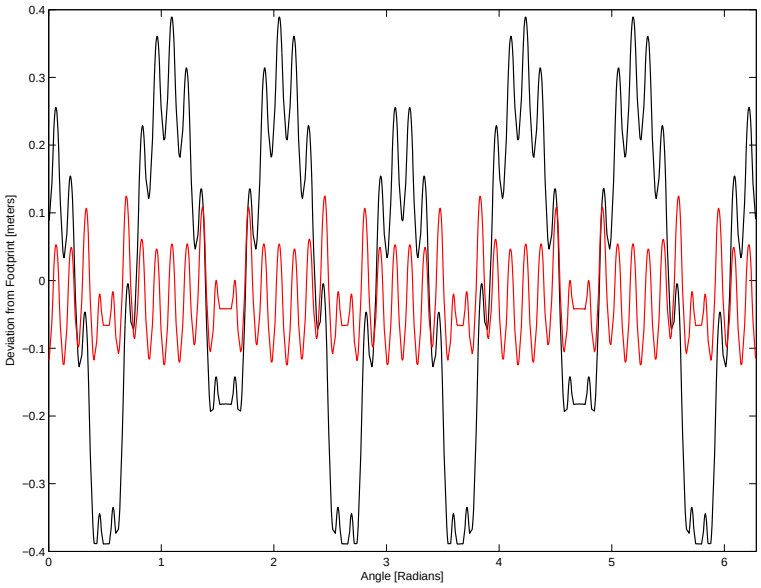

Figure 8: A plot of the difference in radii between the magnet lattice path and the Wilson tunnel. The black line represents the deviations before applying the brute force corrections, while the red line represents the deviations after the brute force corrections. From the plots, we can see that the brute force algorithm was able to reduce the deviation from a span of about 1 meters to less than 0.3 meters.

3 Longitudinal Parameters

The lattice is "isomagnetic", meaning that, everywhere the B field is nonvanishing it has the same value. Assuming $\mathcal{E}_e = 5.0\,\mathrm{GeV}$, we have

$$\rho = 43.4359\,\mathrm{m}, \quad \text{and} \quad B = 0.3840\,\mathrm{T}. \tag{7}$$

The energy radiated per electron per turn is then given by

$$U_0 = 1.273\,\mathrm{MeV}. \tag{8}$$

The characteristic x-ray energy is

$$u_c = 6.384\,\mathrm{KeV}. \tag{9}$$

The longitudinal slip factor is

$$\eta_0 \equiv \frac{1}{\gamma_t^2} = 3.48 \times 10^{-4}, \tag{10}$$

where γ_t is the so-called "transition-γ and μ_s, which is 2π times the longitudinal phase advance per turn, is given by

$$\mu_s^2 = \frac{\mathcal{C}}{c}\,\omega_{\mathrm{RF}}\eta_0\,\cos\phi_0\,\frac{\hat{V}}{\mathcal{E}_e}, \quad \text{or} \quad Q_s = \frac{\mu_s}{2\pi} = 0.0090, \tag{11}$$

where $\mathcal{C} = 765\,\mathrm{m}$, $\omega_{\mathrm{RF}} = 2\pi \times 500\,\mathrm{MHz}$, $\hat{V} = 6\,\mathrm{MeV}$ (assuming half to be provided by each of two cavities) and, for the time being, $\cos\phi_0 = 1$. The total RF power will then be somewhat less than that required for 5 GeV CESR operation.

For separated function lattices, Sands' $\mathcal{D} << 1$, and the fractional energy spread is given by

$$\sigma_\delta = 0.813\,\sqrt{\frac{u_c}{(2+\mathcal{D})\,\mathcal{E}_e}} = 0.65 \times 10^{-3}. \tag{12}$$

This will have to be corrected for the effect of the (relatively weak) combined function bend magnets. The bunch length (needing similar correction) is given by

$$\sigma_{ct} = \frac{\mathcal{C}D_0}{\mu_s}\,\sigma_\delta = 2.92\,\mathrm{mm}. \tag{13}$$

Expressed as a time this is

$$\sigma_t = \sigma_\delta = 9.7\,\mathrm{ps}. \tag{14}$$

Because this figure neglects the possibility of bunch lengthening, it may be unrealistically short, especially for few bunch operation.

Though this is some six times shorter than the x-ray pulses from CESR, it is still a long way from the sub-picosecond "fast timing" frontier the ERL is intended to investigate. At a substantial cost in photon flux, it is possible to obtain

much shorter x-ray pulses by laser "slicing". For example, Ingold et al.[13] have obtained x-ray pulses in the 1 to 10 keV range, with FWHM=140 ps. CESR-X could obtain similar pulses, with greater flux, and at shorter wavelengths, exploiting the possibility of few bunch operation. In order to retain capabilities like these it will be important to retain CESR's current bunch pattern flexibility.

These considerations notwithstanding, the short bunch length capability may be a major nuisance for many applications. There may be excessive higher mode power dissipation and excessive particle loss through Touschek scattering. It is possible, therefore, that one will plan to eventually have a third harmonic bunch lengthening RF cavity right from day one. For most x-ray experiments the bunch fill pattern is unimportant, so the wall heating can be reduced by increasing the number of bunches while holding the beam current constant. The default running condition is likely to have a large number, such as 100, of filled bunches in the ring.

3.1 RF and the Damping Wiggler Option

Most of the parameters in this paper assume that there are no damping wigglers in the lattice. But the 12 wigglers currently in CESR-C could be installed in the CESR-X ring. Since their individual lengths are 1.7 m, four of these wigglers will fit in each of straight sections L2, L4, and L5, all of which have the necessary zero dispersion. Table 1 gives some properties of the resulting ring. Roughly speaking, the wigglers reduce the emittance by a factor of two and (with reduced beam current) increase the brilliance by a factor of three.

The proposed baseline RF layout for two cryomodules, is close to its present position in CESR, as shown in Fig. 9. The existing SRF cryomodules are well suited for the CESR-X needs and will be reused.

The four CESR superconducting cryomodules can operate with an average gradient of 6.2 MV/m, providing total voltage of 7.4 MV, while supplying 270 kW power per cavity. This should be sufficient for all entries in Table 1.

4 Required New and Rebuilt Hardware

4.1 Bending Magnets

The existing CESR operates with eighty-four bending magnets. These bending magnets have constant magnetic fields in the region between the magnetic poles and serve to constrain the electron beam to follow the footprint of the Wilson tunnel; see Fig. 10. To provide the vertical focusing required for vertical stability the bending magnets can be shaped so that the field develops a gradient along the vertical direction, namely $\partial B_x/\partial y \neq 0$. Electrons displaced vertically from the central plane will feel a restoring force. A modest additional bonus of the combined focusing, as in other modern light sources such as APS and CLS, is a 25% or so increase in horizontal damping partition number. This leads

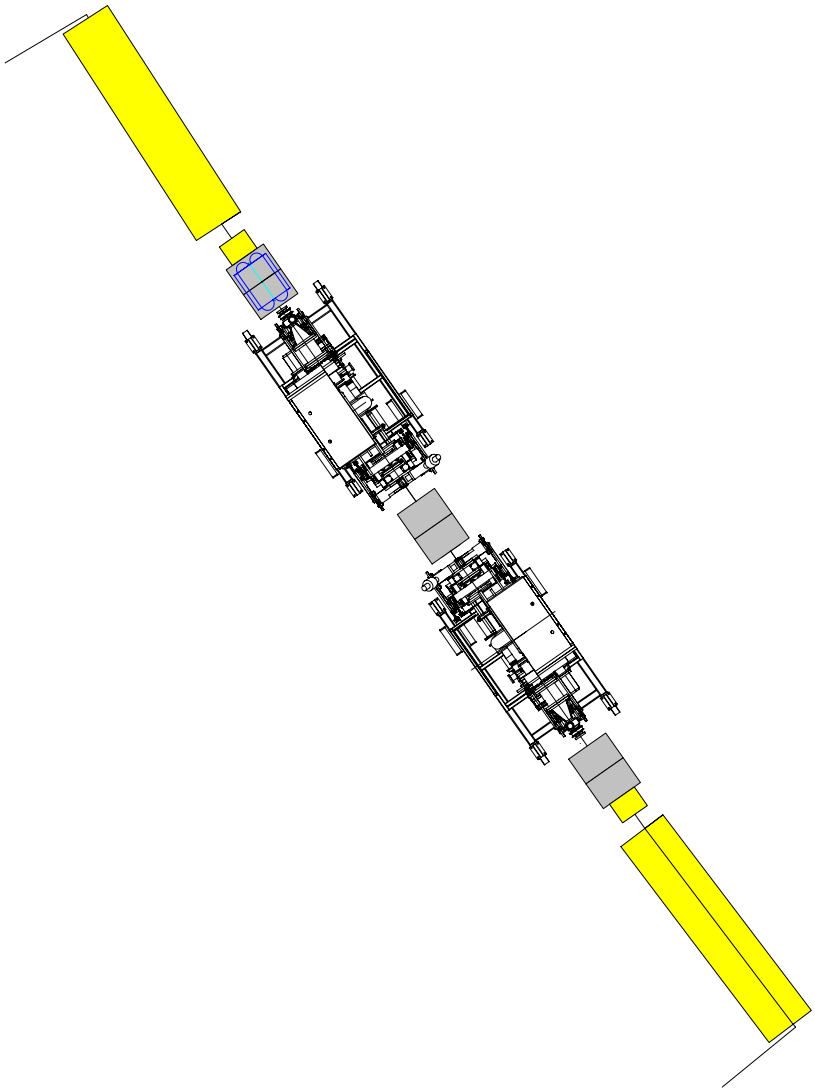

Figure 9: Two adjacent RF cryomodules fit within the straight sections of bend cells, presumeably close to their present west flare locations. A very important, but not yet begun, task, is to design synchrotron light masking for the RF cavities.

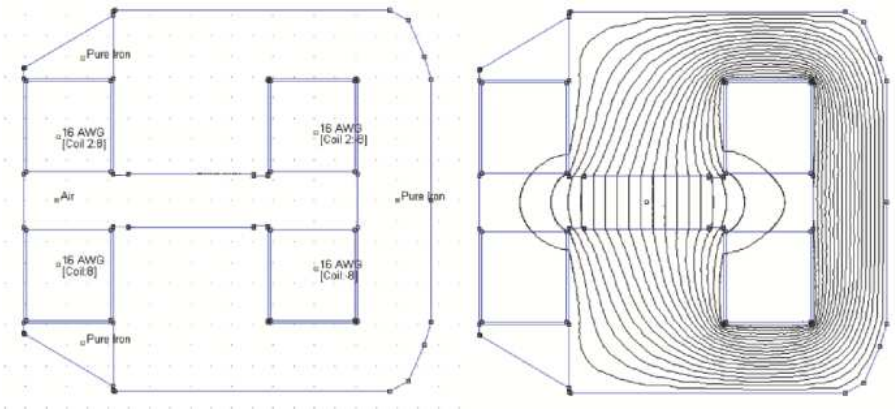

Figure 10: A cross sectional view of the existing dipole bending magnet. The figure on the left shows the composition of the dipole magnet, while the figure on the right shows the magnetic field lines created by the magnet. The density of the field lines is proportional to the magnetic field strength. From the figure on the right, we can see that the region between the magnet poles have a constant density of field lines and thus a constant magnetic field strength. These figures were created using FEMM.

to a proportional reduction in transverse beam emittance[14] and a quadratic increase in x-ray brilliance.

There is, however, the constraint $\partial B_y/\partial x = \partial B_x/\partial y$, which limits the ability for the bending magnets to focus the beam, since any additional focusing in the vertical direction reduces the focusing in the horizontal direction and vice versa. The measure of combined-function focusing is the quadrupole coefficient,

$$K_1 = \frac{\partial B_y}{\partial x}\frac{1}{B\rho}. \tag{15}$$

We found that the optimal value for the proposed CESR-X lattice is $K_1 = -0.080\,\mathrm{m}^{-1}$.

Since the bending magnets are one of the main constituents of the storage ring, much effort has been directed to preserve the magnets to the greatest extent possible. To this effect, we have designed iron crowns, which can readily be attached to the current bending magnets, and which provide the necessary quadrupole coefficient. These crowns were designed using the program Finite Element Method Magnetics (FEMM) [15].

The design of the iron crown is complicated by considerations of ease of production and by specifications of the vacuum chamber, which will be situated between the crowns, see Fig. 11. In order to retain the original components of the vacuum pump system in the vacuum chamber, we preserve a 65mm gap in an area large enough to fit the current pump chamber. As for the remaining area between the magnetic poles, we require a gap of at least 40mm.

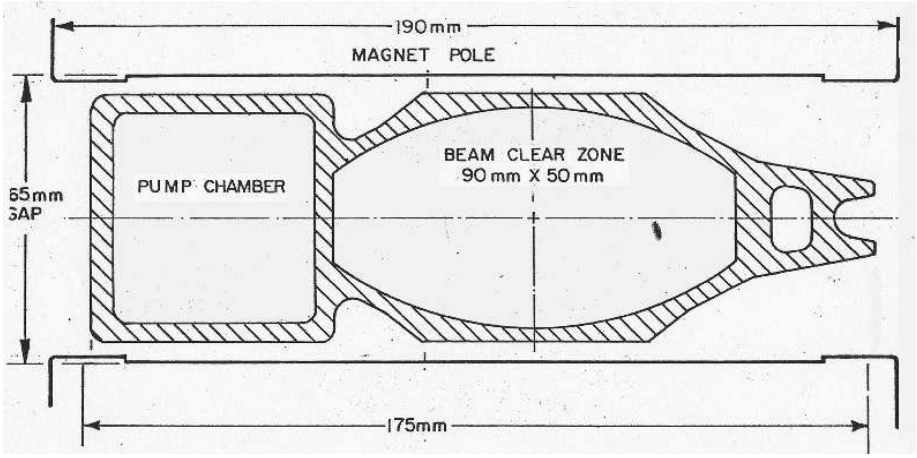

Figure 11: A diagram of the current vacuum chamber situated between the poles of the current bend-magnet. The tip of the vacuum chamber faces the outside of the Wilson tunnel.

Further, we require that our gradient $\partial B_y/\partial x$ span at least a seven centimeter region along the x-axis at $y = 0$, termed the "good field region". Fig. 12 and Fig. 13 show our crown design, which match all of the constraints. Fig. 14 shows the resulting gradient $\partial B_y/\partial x$ when the crowns are attached to the bending magnets. A linear regression of the resulting magnetic field produce the equation $B_y[\mathrm{T}] = 0.385 - 1.366x[\mathrm{m}]$ with an R^2 value of 0.999. Here the good field region spans 7.0cm and is defined as all consecutive points which fall within 0.20% of the value predicted by the regression equation.

Field uniformity in the pump chamber region is considered to be unimportant.

At near light speeds, where $\beta \approx 1$, and with electron energies $\varepsilon_e = 5.11[\mathrm{GeV}]$, Eq. (15), for calculating the quadrupole coefficient can be written as $K_1 = 0.058669\,\partial B_y/\partial x$. Using the slope obtained from our crown design, $\partial B_y/\partial x = -1.366$, we obtain a quadrupole coefficient value $K_1 = -0.080$.

It remains open how the crowns will be held in place. Once the bend-magnets are turned on, the induced magnetic field alone will be more than sufficient to press the iron crowns against the iron laminations.

As shown in Fig. 15, because of the curvature of the central orbit, there is a substantial sagittal dispacement (3.1 cm) at the magnet ends relative to the rectangular magnet core edges. To compensate for this it is suggested that there will be three pole piece crowns (as described earlier in this section) per magnet. Hence, though the vacuum chamber is curved continuously, the magnet pole face consists entirely of plane surfaces.

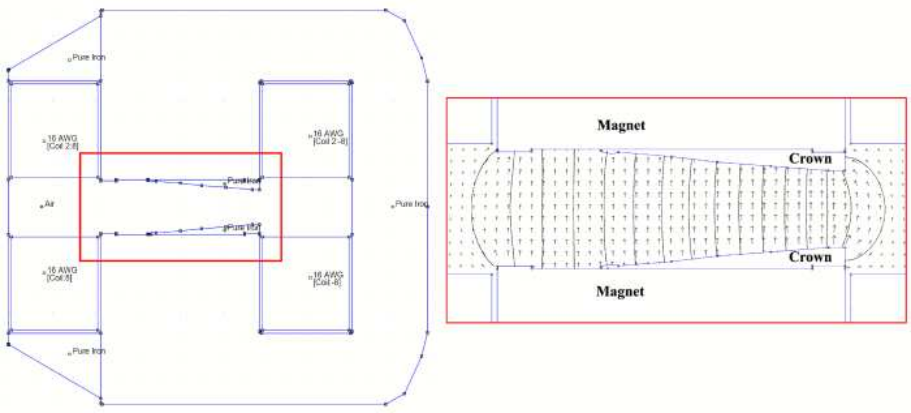

Figure 12: A cross sectional view of the modified bending magnet. The figure on the left shows the composition of the modified bending magnet, while the figure on the right is a close up view of the magnetic field lines created by the magnet. The arrows in the figure indicate the strength and direction of the magnetic field. These figures were created using FEMM.

4.2 Quadrupoles

Most of the quadrupoles in CESR at present have lengths of 0.6 m, bore diameters 80 mm and maximum focusing strengths $K_1[5\text{GeV}] = 0.56\,\text{m}^{-2}$. From Tables 2 and 3 it can be seen that these quads have the correct lengths, and are almost strong enough to serve as the q_1 quads, but not nearly strong enough to serve as the q_{ss} quads. It is tentatively assumed that these CESR quads will be used at the q_1 locations, but with rebuilt coils. (Some of the CESR magnets have already been strengthened in this way.[16]) All the other quads in CESR-X have shorter lengths and need to have substantially larger gradients than any present CESR quads. They will have to be built new. They can, however, have bore sizes reduced to about $80 \times 37/50 \approx 60$ mm, which assumes they are reduced in the same ratio as the vacuum chamber height.

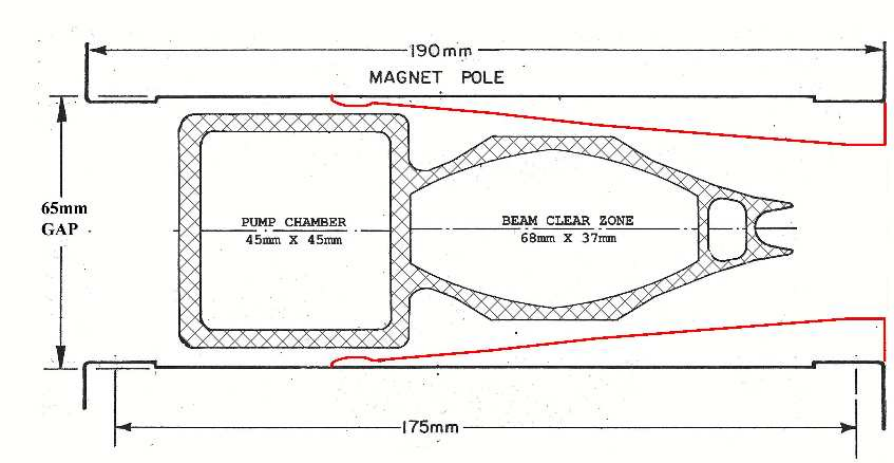

Figure 13: A diagram of a possible vacuum chamber with the proposed crowns superimposed. The sloped section of the crown will provide the necessary quadrupole effect in the beam clear zone, while the level section provides a uniform field for the pump chamber.

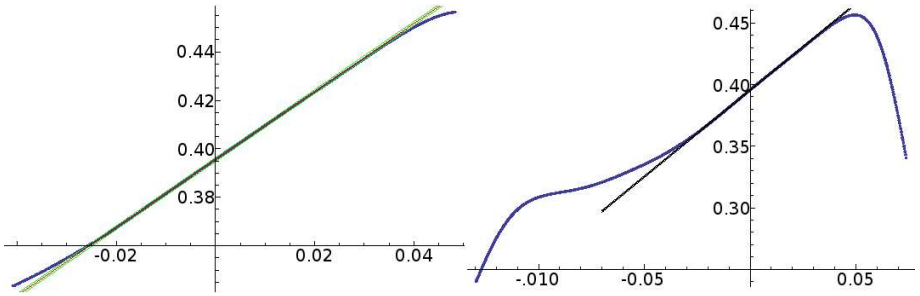

Figure 14: The graph on the left is a plot of the field B_x along the line $y = 0$; linear regressions of both the good field region and uniform field zone are superimposed on this graph. The graph on the right contains a plot of the percentage of error for the regression of the good field region. The good field region for this design spans 7 cm, with errors of less than 0.2%.

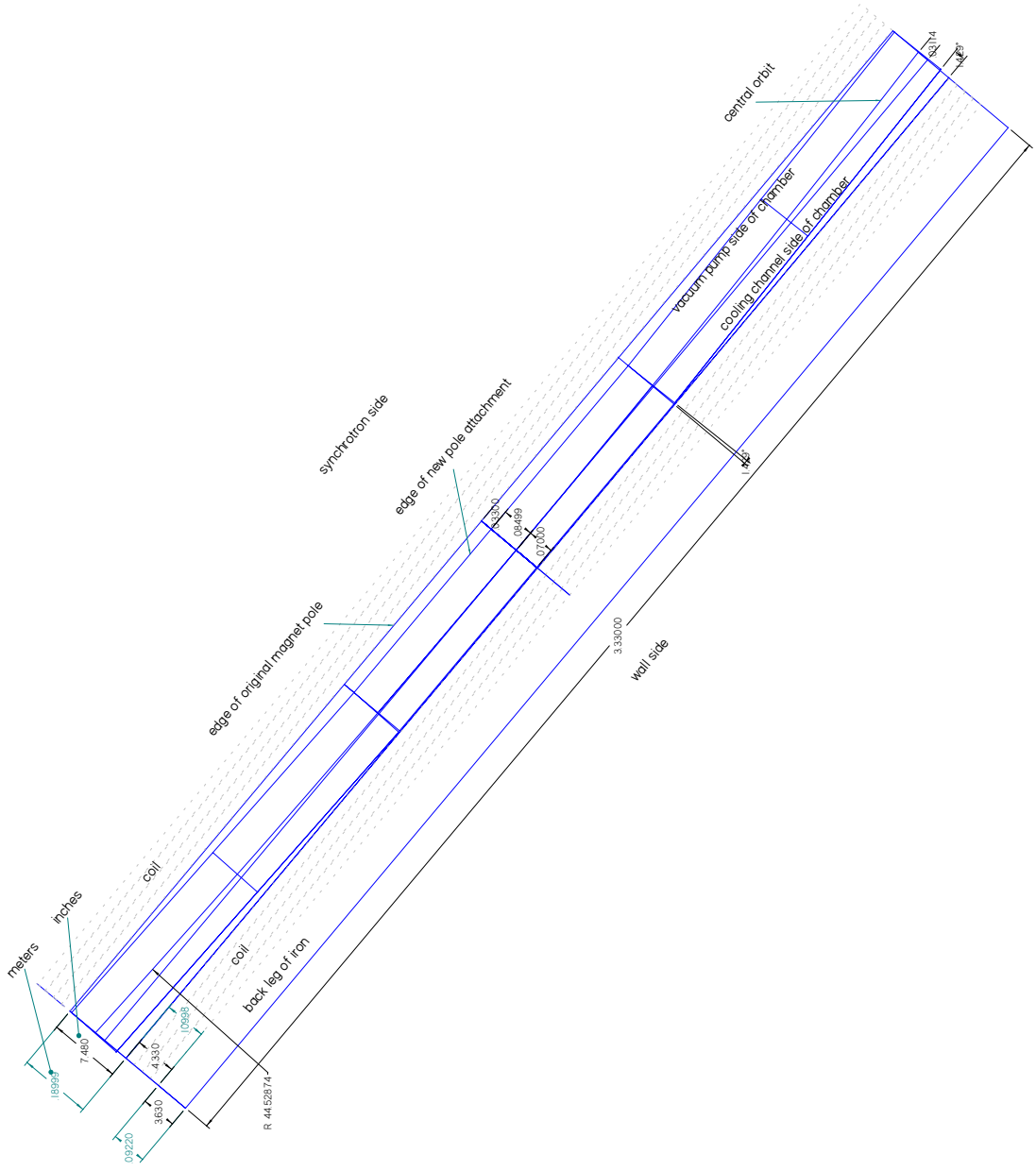

Figure 15: The original uniform field magnets are converted to combined function magnets by the attachment of three pairs of slanted pole inserts per 3.33 m long iron core assembly.

4.3 Vacuum System

Beampipe. Most of the beampipe, including all dipole bending chambers and quad straight pipes, are made of 6061-T4 aluminum alloy extrusions, with a cross-section shown in Fig. 16 The cross section is very similar to the present CESR extrusion, with smaller beam stay-clear aperture to fit inside the modified dipole irons. The distributed ion pump (DIP) channel remains the same as the present CESR extrusion so that all the DIP elements may be re-used.

For the dipole bending chambers, pumping slots will be punched through the wall separating the beam channel and the DIP channel. The size of the pumping slots will be significantly smaller than the ones in the present CESR dipole chambers, to greatly reduce the DIP DC field "leakage". The extrusions with pumping slots will then be formed to the required bending radius, with appropriate straight sections on both ends. The ends of the dipole chamber, with the DIP channel machined off, will be terminated by one of the following options: (A) To be welded to flange with explosion-bonded aluminum to stainless steel (Al/SST) transitions; (B) To be welded to a RF-shielded sliding joint; (C) To be welded to other transition pieces for various special components (such as RF-shielded gate valves, beam current monitor, etc.); (D) To be welded to another dipole chamber directly.

The bending radius of 43.44 m is much smaller than the "normal" bending radius of 87 m in the present CESR, but still larger than the "hard-bend" of the present accelerator. With proposed 300 mA maximum beam current, the cooling channel similar to the current one will certainly be enough to handle the power load from the synchrotron radiation generated from the dipole magnets.

Key Vacuum Components. There are many key vacuum components that are necessary for the CESR-X vacuum system, and that have significant impact on the cost of the CESR-X conversion. Particular attention must be paid to the beam impedance and/or higher-order-modes (HOMs) loss of the vacuum components, as the proposed electron bunch length is much shorter than at present. However, this effect may be alleviated by much smaller bunch peak current with more bunches, as compared to the present CESR. Additionally, the limitation in the present CESR of supportting a limited number of bunches due to the two stored beams in a single vacuum chamber will be removed in CESR-X.

Sliding joints (SLDJTs). A SLDJT with proper RF-shield design is needed between any two dipole chambers, to handle thermal expansion of the vacuum chambers, and to facilitate the chamber installation. Candidates for the RF-shield design include CESR design, KEK-comb design, PEP-II design and PAL design. HOM power loss, and/or beam impedance calculations are needed to decide on a design, though it is somewhat desirable to use the present CESR design due to familiarity of their machining, assembling, hardening surface coating, etc. If suitable, especially in the insertion-device-free sections of CESR-X, some of the currently installed SLDJTs may be re-fitted (with appropriate transitions).

Beam Position Monitors (BPMs). The majority of the BPMs will be button-style. A design similar to the present CESR BPMs should be suitable, probably with smaller pickup buttons, due to smaller beam aperture.

RF-shielded Gate Valves (GVs). Similar to the present CESR, the CESR-X vacuum system will be sectored by RF-shielded GVs. We expect to re-use all the GVs installed in CESR. A pair of tapers will be added to allow smooth beam aperture transition from the new CESR-X extrusion to the GV opening. With a conservative 10:1 transition, the pair of tapers requires only 0.25 m space along the beam direction.

X-Ray Beamline Starting Components. Each proposed X-ray beamline must be equipped with a crotch. A design similar to the present G-line crotch (which is capable of handling 500 mA beam current at 5.2 GeV) is likely to be used.

The photon beamline after each crotch must also be equipped with two photon beam stops and an all-metal gate valve (no RF-shield). One of the beam stops is required for safety and these components need to be installed on day one, even if the down-stream X-ray optics is not installed. Current CHESS photon stops and GVs are suitable (though more are needed).

X-Ray Insertion Devices. There are at least two types of IDs, undulator vacuum chambers (UVCs) (with out-of-vacuum magnets) and in-vacuum undulators (IVUs). A design similar to the current G-line wiggler vacuum chamber will be one of the reference designs for the UVCs. Another example is the extruded aluminum ID chamber with 5 mm vertical beam aperture used at ESRF. Shown in Fig. 17 is an IVU design for PLS, for reference. The placement of the IVU probably will be limited by the tunnel space.

Photon Absorbers and Masks. Photon absorbers and/or masks are required wherever a section of outer vacuum wall is "missing" or needs to be shadowed, such as at an IVU.

Beam profile monitors. In the present CESR, two types of synch-light beam profile monitors are used. Beam transverse size is measured using in-vacuum beryllium mirrors and optical interferometers at Q23E/W. Beam bunch-length measurement is done using a in-vacuum copper mirror and a streak-camera at L3. We assume similar devices will be needed for CESR-X.

Beam Injection Chamber. A new injection chamber with thin titanium injection window is most likely required. Its design should be conceptually similar to the present CESR injection chamber.

Vacuum Pumping. The main pumping system will consist of distributed ion pumps (DIPs) in the dipole magnets and noble diode lumped ion pumps (LPs) in the straight sections, in an arrangement very similar to the present CESR. The much smaller pumping slots proposed for the CESR-X dipole chamber will reduce the DIP pumping speeds significantly. However, as the operational experiences in the CESR-c has shown, the well-conditioned (after over ¿100 Amp×hr beam dose) aluminum beam pipes become very effective getter pumps to keep average vacuum pressure below 10^{-9} Torr with 300 mA stored beam.

The installed DIPs and LPs in the present CESR can be re-used for the CESR-X conversion. No purchase of new ion pumps is needed, though partial upgrade of ion pump controllers is necessary.

At locations (such as insertion devices, photon-absorbers, etc) where ion pumps are not suitable due to limited space or due to sensitive to stray magnetic field of the ion pumps, getter pumps (TiSPs or NEGs) will be used. Thin NEG coating may also applied to certain vacuum chambers (such as ID chambers with very small vertical aperture) for pumping. The NEG thin film deposition can be done by SEAS, Inc.

Vacuum Instrumentation. More vacuum instrumentation should be planned for CESR-X. Total vacuum pressure will be monitored by cold-cathode ion gauges (CCGs, MKS Model 421) (roughly every 5 meters, or ∼150 CCGs). With MKS Model 937A CCG controllers, these gauges are capable of measuring pressure as low as 10^{-11} Torr.

Every vacuum sector must be equipped with a residual gas analyzer (RGA) for leak-checking and vacuum system diagnosis.

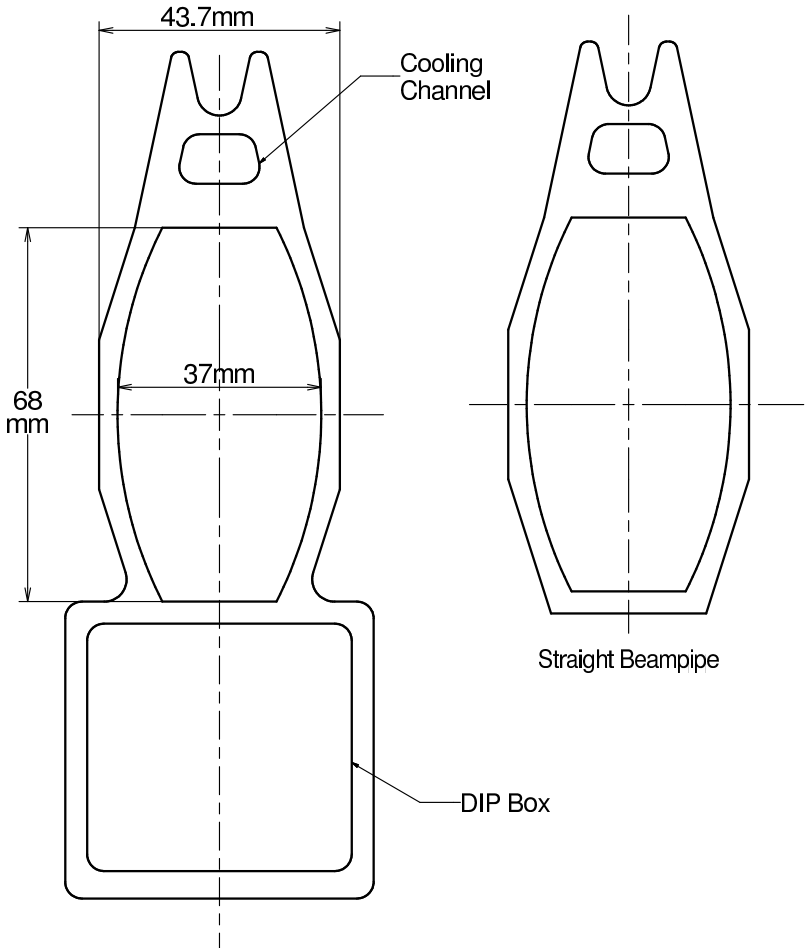

Figure 16: . Cross-section of the aluminum extrusion. For straight sections the DIP box will be machined off allowing the tube to pass through quad and sext magnets.

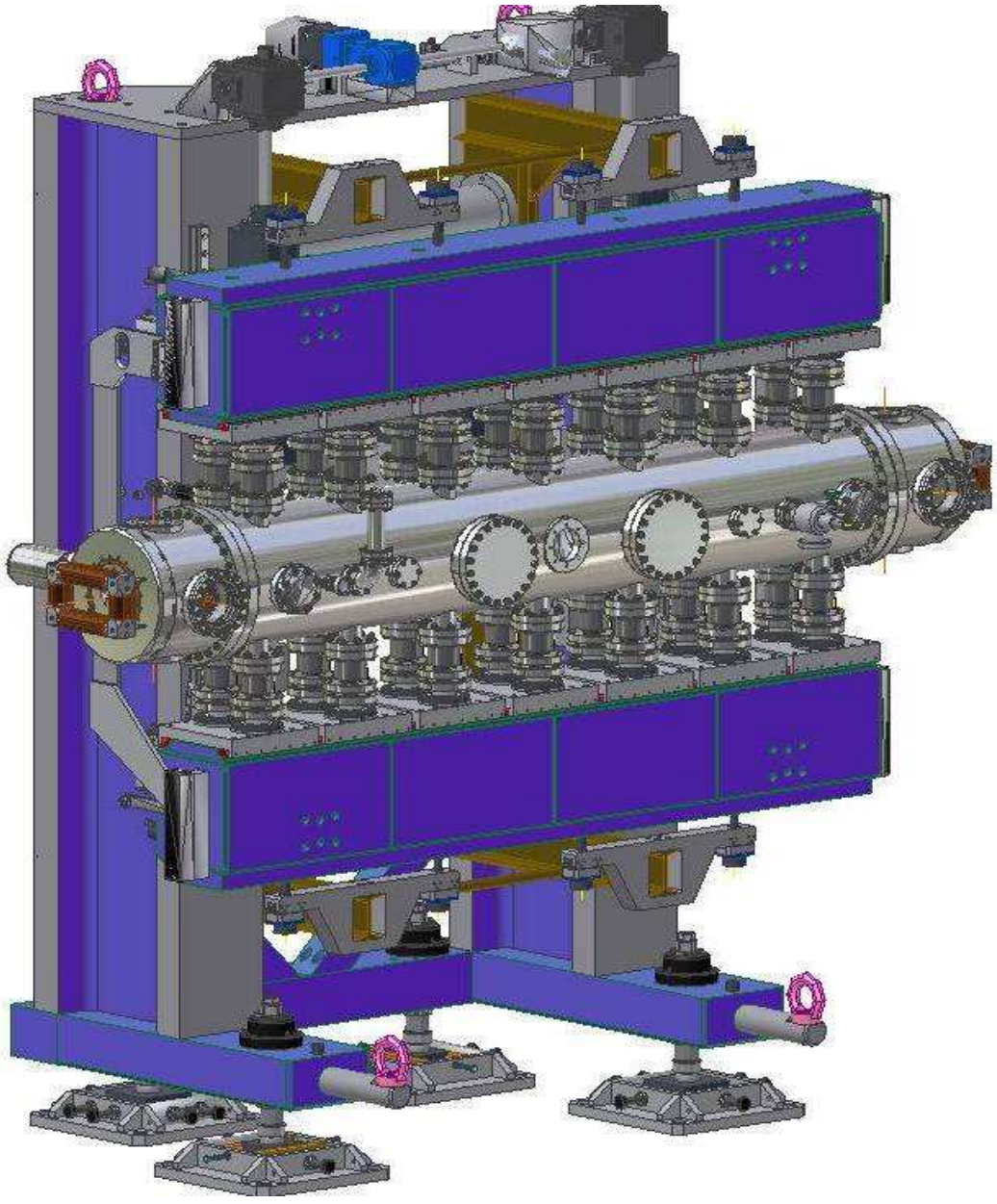

Figure 17: . In-vacuum-undulator design for Pohang Light Source.

5 Notes on Costs

5.1 General Comments

It seems appropriate, when estimating costs, to separate them into two major categories: costs needed to upgrade the machine, and costs needed to build the x-ray beamlines (which also includes the additional cost in civil engineering and construction incurred by the x-ray beam lines and stations (re)arrangement and extensions to Wilson Laboratory building). Eventually the latter costs will surely exceed the former. With CESR-X being an "x-ray factory" the total cost will be a constant term plus a term proportional to the number of beamlines. In this report, it is only the constant term that will be estimated. These are the costs required to convert the present CESR to a machine with the same energy and beam current but with transverse emittances improved by a factor of fifty or so in each plane.

Of course the potential of CESR-X to produce actual beamlines with brilliance some four orders of magnitude higher than CESR, needs to be demonstrated as part of this report. But the x-ray beamline costs for doing this are not being included.

Easier than bottom-up cost estimating is to estimate costs relative to other accelerator projects. One crude estimate was included in reference [9]. To a large extent building CESR-X will just be a repeat of building CESR in the first place. Taking account of inflation, the costs can be referred back to the (well known) original CESR costs. By that method of costing, the cost of CESR-X magnets, magnet supports, vacuum chamber and beam monitoring was estimated to be \$8 million. This can be regarded only as a lower limit, both because many ingredients have not been included and because the inflation factor used (namely 3.3) has been said to be low for the highly technical components needed.

Another comparison can be made with the SPEAR upgrade, completed in 2004, at a total final cost of \$58M.[17] This upgrade, from SPEAR-2 to SPEAR-3, was very similar, both in motivation and in scale, to what is being proposed here; an existing ring was dismantled and replaced by a new ring on the same footprint. With the SPEAR circumference being a factor of three less than CESR, the CESR upgrade might seem to be substantially more costly, but the CESR upgrade is more modest in several ways.

The dipole counts are SPEAR, 36-new, CESR-X, 48-old, but modified. The quadrupole counts are SPEAR, 94, CESR-X, 169, of which about half are taken from CESR. As it happens, because of its shorter cell length and similar bore size, the SPEAR and CESR-X quads would be pretty much interchangeable, in spite of the SPEAR energy being less by 3/5. (The bore size for the SPEAR quads is 70 mm, somewhat larger than the 60 mm bore size thought to be minimum for CESR-X.) These quads would have a similar price tags. The SPEAR-3 costs for magnets and their power supplies was $8.4 + 3.1$ \$M. The CESR-X magnet costs will be far less because so many magnets and a substantial fraction of the magnet powering will be obtained directly from CESR.

Also, SPEAR-3 has a brand new RF system, costing 4.5 $M, while the CESR RF will be essentially unchanged.

The most expensive part of the upgrade of the machine itself will be the vacuum chamber. The SPEAR-3 vacuum system cost was 13.0 $M. However, for CESR-X, much of this equipment will be reused from CESR. In particular, since the ion pump chamber dimensions and magnetic fields are unchanged, the CESR pumps can be used in CESR-X. As explained previously, except for six straights, CESR-X has a superperiodicity of 42. About two thirds of the ring amounts to being a "return loop", not used for x-ray sources. This section can largely be populated with vacuum and beam monitoring equipment from the present CESR.

Unfortunately the cost comparison with the SPEAR upgrade is clouded by a far more important uncontrolled variable. The SLAC and CESR "styles" are utterly different. The SPEAR-3-upgrade report has some 500 authors, while the CESR-X upgrade would require fewer than 100. The ideosyncrasies of different laboratory accounting practices makes direct cost comparison all but impossible.

An independent way of estimating costs is to refer to the recent cost estimate, made by ACCEL, for that portion of the Cornell ERL that resembles the proposed CESR-X upgrade. For example the costs for new CESR-X quadrupoles can be estimated from this source – basically, quadrupoles cost 10 $K per magnet. This will be the largest magnet expense for CESR-X. The results are shown in Table 3.

The ACCEL report can also be used to (crudely) estimate the cost of vacuum chambers. Their total vacuum chamber cost for a beamline of length 1628.5 m length is 7 $M. Derating this by a factor 768/1628 to account for the different lengths, one obtains 3.3 $M as an estimate for the CESR-X vacuum system. This figure needs to be corrected both up (to account for special vacuum requirements in the ring) and down (to account for savings from salvaging CESR equipment). Since the latter correction is certainly greater, the figure 3.3 $M is a kind of upper limit for this estimate – notwithstanding the fact that it is some three times less than one obtains from the SPEAR comparison. If one insists on retaining SPEAR costs, but breaks them down in greater detail than has been indicated here, one obtains 9.3M as an upper limit for the vacuum chamber cost.

5.2 Magnet Counts

The number count of magnets, and their parameters, are given in Table 2. Quadrupole costs are estimated in Table 3.

parameter name	unit	value
number of bend cells		42
number of FODO cells		14
number of half bends		12
number of full bends		36
L_b	m	6.498
θ	rad	$2\pi/42$
ρ	m	43.4359
l_{q1}	m	0.8
l_{q2}	m	0.4
$l_{full\ ss\ quad}$	m	0.8
l_{sext}	m	0.3
$l_{bend\ cent.\ qb}$	m	0.05
$ld1$	m	2.85
$ld2$	m	0.206664
lss	m	2.009505
N_{q1}		42
N_{q2}		84
$N_{q_{ss}}$		22
$N_{q_{ss}/2}$		12
`k1[q1]`	1/m	-0.450848*8/6
`k1[q2]`	1/m	0.698042*8/6
`k1[qss]`	1/m	0.836556*8/6
`k1[b]`	1/m	-0.0804032
`k2[s1]`	$1/m^2$	-11.5*3/2
`k2[s2]`	$1/m^2$	13.8*3/2

Table 2: Magnet parameters. The magnet lengths roughly include end effects and the strengths are roughly scaled up to compensate. $ld1$ and lss are the drifts available for insertion devices, RF, etc. In all cases, the insertion devices can be paired into elements at least twice this long

identification	iron length m	gradient m^{-1}	number	unit cost $K	total cost $K
q1: new coil	0.6	0.60	42	3	126
q2: new	0.3	0.94	84	10	840
qssh: new	0.3	1.12	12	10	120
qss: new coil	0.6		22	3	66
qtl: new			9	10	90
total			169		1242

Table 3: Quadrupole parameters and counts, with costs obtained from a recent report prepared by ACCEL for the proposed Cornell ERL.

6 X-Ray Beamlines

6.1 CESR-X-Specific Undulator Design

As described earlier there are four types of undulator line: **A**,**B**,**C**, and $\mathbf{C_2}$. Numbers of, and properties of these lines are given in Table 4 and their locations are shown in Fig. 18.

6.2 Dual Canted Undulator X-Ray Lines

The $\mathbf{C_2}$ lines are patterned after the "dual canted undulator lines" at the APS lab [18]. The APS standard straight sections support a magnet sequence B,U,(-B,-B),U,B, where B stands for (specially-added) 0.5 mrad bends and U stands for 2.4 m undulators. This yields two half-strength beams, separated by 1 mrad.

In CESR-X, the bends can be achieved (with no extra magnets) by radial displacement of adjacent q1 and q2 quads. The two undulators would be "CESR-X standard", slightly longer than the APS undulators. Even with equivalent B-value equal to 2 mrad (four times as strong as APS) there is no visible effect on the Twiss functions of the CESR-X ring in switching one cell from **C** to $\mathbf{C_2}$. Distortion of the dispersion function is more noticeable; see Fig. 19; but still acceptable for this unnecessarily large x-ray beam separation. The same precision quadrupole translators can be used to help line up the **C**-line when full-length undulator operation is required.

6.3 Beamline Parameters

Beamline identifications, properties, and parameters are shown in the following tables and figures.

Table 4: Parameters of the easily accessible CESR-X beamlines. $E_e = 5\,\mathrm{GeV}$. $I = 300\,\mathrm{mA}$. Any of the **C** lines can be configured as canted undulator 2.85 m undulator lines, called $\mathbf{C_2}$, as at APS. For the **C** column, the undulator lengths have been reduced by 0.5 m to allow for transition sections.

parameter	unit	**A**	**B**	$\mathbf{C/C_2}$
number of lines		2	1	12
number of segments		6	4	2
segment length	m	2.053	2.053	2.85
total length	m	12.3	8.2	5.7
$< D_x >$	m	0	0	0.17
$< \lvert D'_x \rvert >$		0	0	0.03
$< \beta_x >$	m	3.5	3.5	10
$< \lvert \beta'_x \rvert >$		3.5	3.5	7
$< \beta_y >$	m	3.5	3.5	10
$< \lvert \beta'_x \rvert >$		3.5	3.5	5
$< \mathcal{H} >$	mm	4.8	4.8	4.8
ϵ_{x0}	nm	4.1	4.1	4.1
J_x		1.27	1.27	1.27
ϵ_x (effective)	nm	3.2	3.2	$\sim$5
$\mathcal{B}_{1,\max}$	convent-	1.9910	1.32	2×0.234
$\mathcal{B}_{3,\max}$	ional	1.2110	0.807	2×0.148
$\mathcal{B}_{5,\max}$	units	0.9113	0.608	2×0.111
$\mathcal{B}_{7,\max}$	$\times 10^{21}$	0.7116	0.474	2×0.087

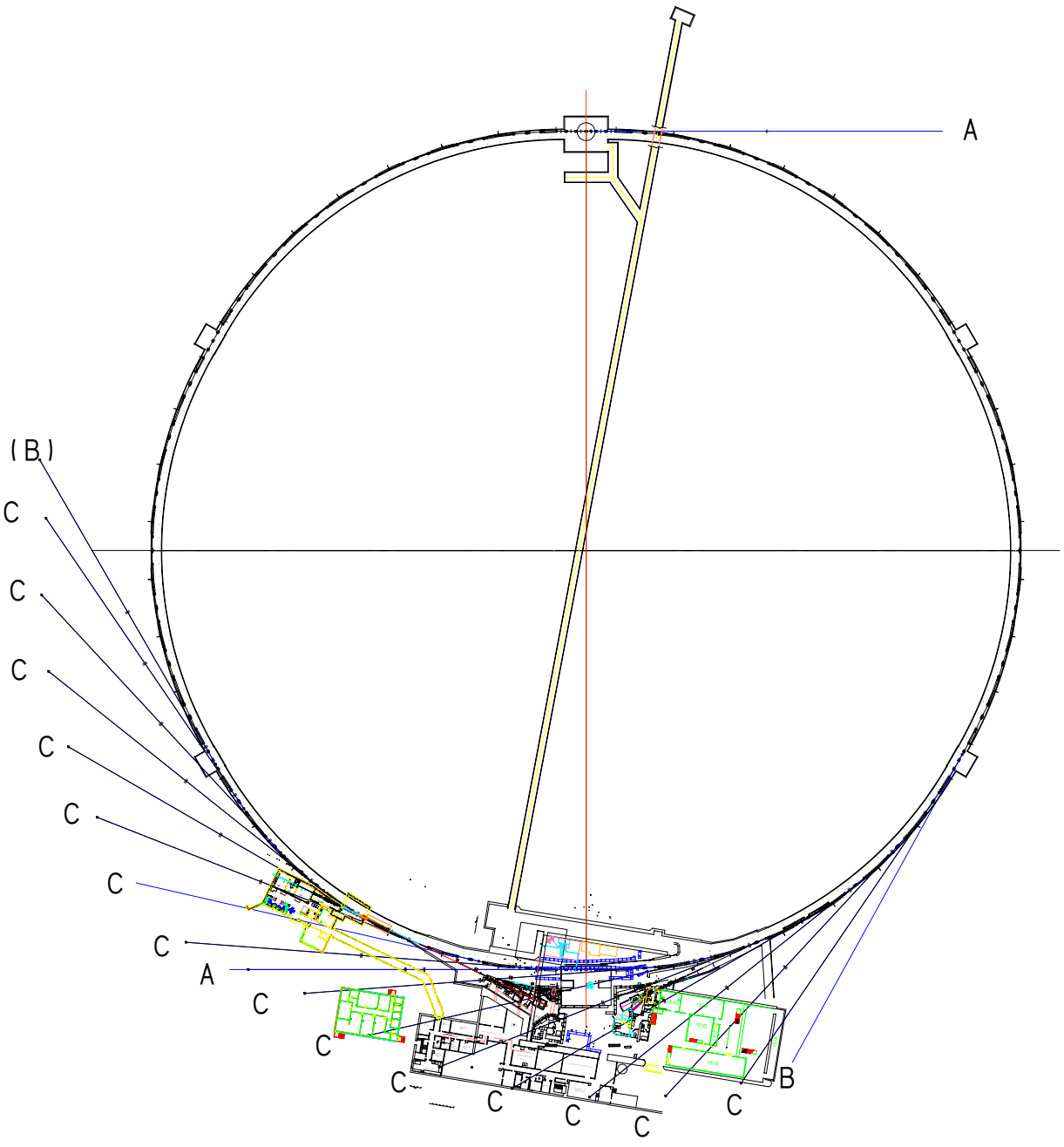

Figure 18: Candidate X-ray beamlines of types A, B, and C (see Table 4) that point more or less toward the present laboratory.

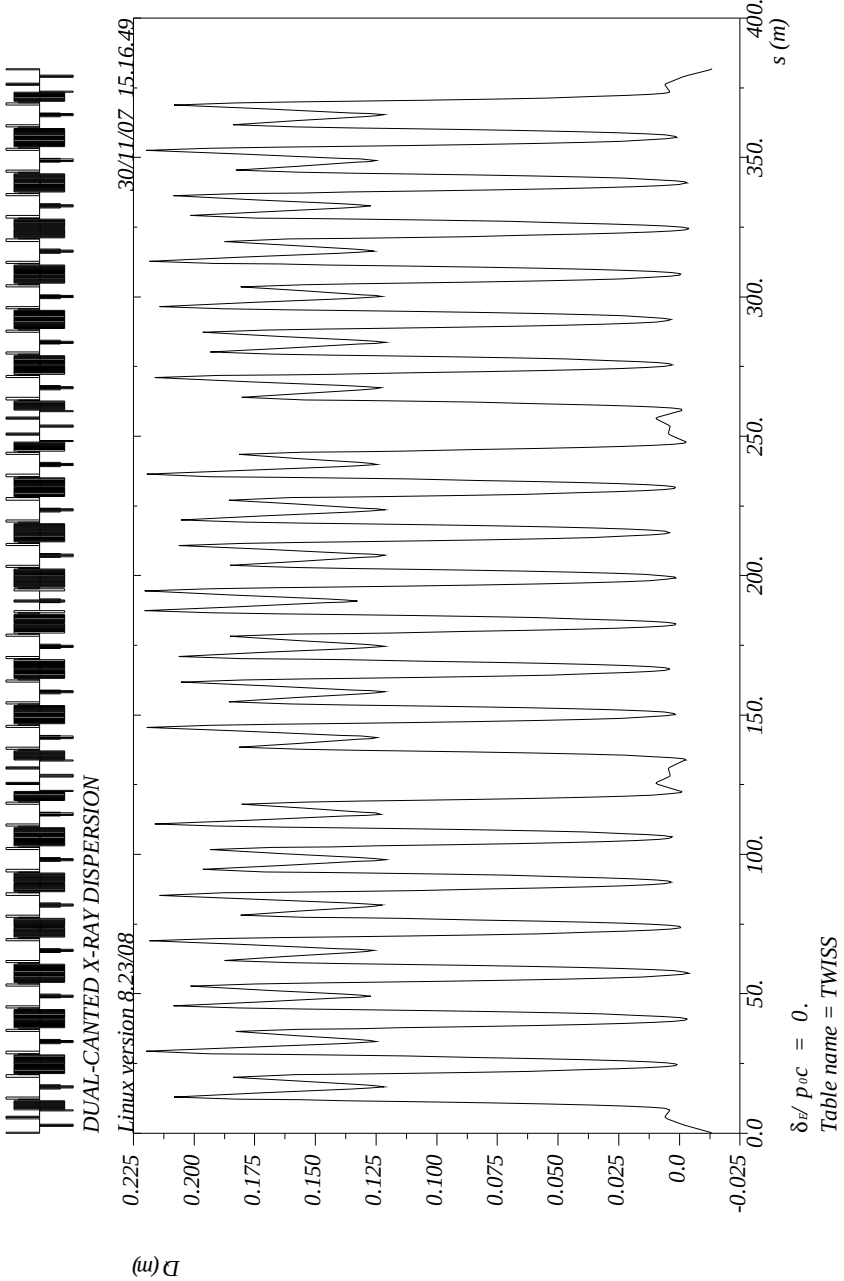

Figure 19: Dispersion function variation (compared to Fig. 4(b)) resulting from the conversion of a C-type line into a C_2-type line, to produce dual canted lines with separation of 4 mrad – this is some four times larger than is expected to be required. The Twiss functions are unaffected by the change.

Harmonic	Energy keV	Brilliance standard units
1 @ peak	4.86	1.3×10^{20}
3 @ peak	9.17	1.06×10^{20}
3	∼20	3.9×10^{19}
5 @ peak	15.28	8.39×10^{19}
5	∼30	2.0×10^{19}

Table 5: Predicted brilliance for 5 GeV, 300 mA operation of C-type beamliness. These numbers are consistent with Fig. 1.

7 Science Opportunities With CESR-X

7.1 Introduction

CESR-X will be a first rate source for experiments that demand high brilliance and/or very high flux, especially at energy above 10 keV, in a narrow bandwidth, on small samples. Obvious applications include protein crystallography, diamond anvil cell (DAC) based high pressure science, inelastic x-ray scattering, and resonant scattering at hard x-ray absorption edges. In addition, the relatively short x-ray pulse length (10 ps RMS) when compared to other sources (40 ps for APS in standard operating mode, and for PETRA3, 20-70 ps at ESRF, and NSLS-II aims for 11 ps) would be very useful for studying short lived excitations (eg. laser pump/x-ray probe experiments), and for spectroscopic study of spin dynamic that utilize magnetic resonance[19]. Although one A-type CESR-X "super beamlines" is ideally located for long ID applications, we will discuss science enabled by the numerous "standard" C-type beamlines where two IDs can operate in tandem (1 beam) or canted (2 beam) arrangements. With the innermost sextipoles removed and 1/2 meter/ID reserved for transitions, flanges, etc, each ID can be 2.65 meters long. If the nominal ERL ID (22 mm period, in-vacuum PPM) is used, this space fits two 120 period devices with combined brilliance (without phase matching) given in Table 5.

For example, the brilliance is closely matched to that expected for IXS-CDT, a state-of-the-art beamline being built at APS for inelastic scattering.

Let's take a closer look at some examples of science for CESR-X.

7.2 Inelastic X-ray Scattering

These experiments measure the spectrum of excitations in solids and liquids by recording x-ray energy loss; sensitivity to excitation length scale is selected by the scattering angle. The dynamical structure factor $S(Q, \omega)$ of phonons, magnons, plasmons, etc can be measured. Spectrometer resolution (including monochromator + analyzer) required for electronic excitations is sub-eV; while sub-meV resolution is needed to study lattice excitations. These are flux driven experiments where the incident energy is scanned with resolution down to 10^{-4} eV. As discussed above, the standard CESR-X beamlines will have bril-

liance comparable to state-of-the-art IXS beamline worldwide. There is only one optimized beamline at each hard x-ray sources where this work is done. So a CESR-X capability would be very welcome. High brightness is essential for forefront applications when, for example, measurements are made inside a diamond anvil cell. The need for high energy photons is driven by several factors including analyzer resolution. One works very close to 90° Bragg angles using high order reflections to achieve meV resolution. The signal is proportional to scattering volume and the DAC and other special sample environments require hard x-rays.

7.3 High Pressure Science

A frontier area in high pressure research is in the understanding of structural phases of light elements and mixtures. The search for metallization of hydrogen is an extreme example. In a DAC, the diffraction signal depends on the number of photons/second illuminating the sample, but useful sample volume is limited to the region of uniform pressure. The diffraction signal (e.g. in angle dispersive x-ray diffraction) is proportional to $I_0(\text{photon}/s/\text{area}area)Z^2N$ where N is the number of atoms illuminated. Assuming sample thickness scales with DAC aperture D, $N \approx \rho D^3$ where ρ is sample density, the signal $\approx I_0 Z^2 D^3$. From experience and analysis (by Ruoff et.al.[20]), diamond anvil cell (DAC) aperture D is inversely proportional to pressure. Therefore incident flux I_0 must increase like P^3/Z^2 to maintain good signal as the pressure increases and for sample composed of low Z elements. An ideal source for this work is one that produces high brightness at 20-30 KeV. Presently HP beamlines at APS utilize a single APS undulator A producing brilliance $\sim 10^{19}$, 2 to 4 times less then the (C-type) tandem CESR-X source. Undoubtedly, a major benefit of CESR-X will be to maintain (and expand) the long standing expertise in high pressure science at Cornell.

7.4 Resonant Scattering in Pump-Probe Mode

An example that emphasizes the positive impact CESR-X can have in paving the path for a Cornell ERL is in pushing the limits of resonant diffraction (RXD). This technique is exquisitely sensitive to how electrons (and holes) are shared between atoms in crystals; it is used to determine the nature (structure) of electronic, magnetic and orbital ordering. A new RXD "pump-probe" technique is being developed to study how chemical bonds respond to atomic displacements when molecules making up a lattice vibrate in phase (coherent optical phonons). In contrast to near-visible Raman spectroscopy that measures lattice vibration frequencies, linking them to specific normal modes, these RXD experiments will sense wavefunction modulation as bonds vibrate. Near a phase transition Raman lines shift, broaden, and (dis)appear indicating changes in symmetry and in interatomic potential. RXD experiments should provide direct evidence on how electron and phonon interact to affect (and be affected by) phase transitions. In pump-probe RXD a laser "tickles" the sample by impulsive excitation

when the pulses are short compared to the period of phonon vibration and the sample response decays quickly compared to the time between x-ray pulses. At a controlled delay after laser excitation, the bond is probed by RXD at reflections normally forbidden by the crystal symmetry. Certain of these reflections can be excited when the x-ray energy is tuned to an absorption edge because the resonance can distinguish atoms related to one another by glide plane (or screw axis) symmetry. The laser electric field is the same at all molecules within the illumination volume so it can impose a new symmetry (breaking) condition that affects these resonant reflections.

Because pulses from a future ERL can be short compared to the lifetime of these coherent vibrations, we can look forward to dynamical studies of vibrational decay, and possibly to "coherent detection[21]. In the mean time, the time structure of CESR-X ($\sim$10 ps pulses separated by $\sim$2 ns) is favorable for studying how ultra-short laser pulses modulate the energy, angle, and polarization dependence of RXD. In this case, when x-ray pulse and phonon lifetime are comparable, the x-rays sample a fully excited lattice. This work could lead to a new time domain spectroscopy of interactions between lattice vibrations and electrons that participate in chemical bonding, charge transfer, and magnetism. In principle, stretched and bent molecules, distorted lattices, and out-of-equilibrium structures could be directly characterized in stop-action time slices.

7.5 Pair-Distribution Function (PDF)

Though it is an old technique, motivated by a Debye formula from 1915[22], the pair-distribution function (PDF) has generated considerable recent interest, mainly for the study of "crystallographically-challenged" and amorphous materials. These applications have been made practical by the availability of modern computational power. The PDF topic is thoroughly discussed in a book by Egami and Billinge[23] and (more concisely) in a review article[24]. The technique can be applied both to x-ray and neutron diffraction with the latter being especially useful for establishing the structure of molecules containing low Z atoms. However the superior resolution achievable with x-rays makes them appropriate for the study of glasses and other materials in the border region between crystalline and non-crystalline.

Though by no means a "killer ap", the PDF approach is particularly appropriate for CESR-X for two reasons: the method requires very hard x-rays – at least 50 keV, and preferably higher – and part of the resurgence of interest in the method stems from pioneering measurements at CHESS [25]. The PDF approach, because of its need for bright high energy beams, has subsequently migrated, for example, onto a PDF-dedicated beamline 11-ID-B at APS. Additionally, PDF technique benefits from narrowly collimated beams. Both of these features are the strengths of the proposed CESR-X.

7.6 Measurement of Transient Intermediates Along the Folding Pathways of Proteins, RNA or DNA

The Folding Problem. Proteins, RNA and DNA, the macromolecules most commonly associated with life, "fold" into specific shapes or structures that enable their biological functions. The overall size of the folded structure is typically some 10's of Å's. Many of these molecules, notably RNAs, self-assemble hierarchically; small, structured "domains" form and serve as scaffolds for subsequent folding events. It is of great interest to biology, physics and medicine to dissect the folding pathways, essentially "watching" these molecules self assemble. This task is non-trivial because of the wide range of length and time scales involved. To achieve this goal, a measurement tool must be developed with sensitivity to length scales from a few through tens of Å's, and time scales as short as microseconds.

Solution x-ray scattering is an ideal method for probing the length scales of interest; however there are two great challenges associated with adding time resolution. First, the scattering intensity is roughly Gaussian at small angles (SAXS) with maximum in the forward direction. Changes at low angle are related to the largest distances in the sample, thus, although it is relatively straightforward to measure overall size and shape of static macromolecules, with x-ray intensities available from a laboratory source, it is quite a challenge to consider adding the variable of time. In real time measurement, time resolution equals the length of the x-ray exposure and a synchrotron is required to measure on time scales less than minutes. Real time measurements are still challenging: even at CHESS's high intensity G-line where a minimum exposure time of 50 ms is necessary to obtain measurable signal. Since folding events begin on the microsecond time scale, the second challenge is to find a strategy that supercedes real time measurement.

For nearly ten years, the Pollack lab has been using "continuous flow mixers" as an alternative to "real time measurements". Our methods, plus those newly developed by other groups, have enabled measurements of folding events beginning on the microsecond time scale. However, because these mixers typically use very small sample volume, they require the more brilliant x-ray beams available at 3rd generation sources. It is now relatively routine to measure changes in the radius of gyration of folding samples with sub or low millisecond precision.

A formidable, new frontier in time-resolved solution scattering involves development of new methods to obtain good quality data at larger scattering angles, in the so-called wide angle x-ray scattering (WAXS) regime. At wide angles, structural changes occurring on length scales of 1-10 Å can be determined, allowing measurement of the formation time of the small structural units so vital to biology, such as helices and sheets. Work by other groups (Makowski for example) at APS has begun to explore the power of static (non-time-resolved) WAXS for sensing more local features of proteins, such as secondary structure. However, even at a source as bright as APS, these measurements are challenging because the scattering falls off very rapidly above $1/2\text{Å}^{-1}$. An x-ray source with very high intensity at higher energy has the potential to meet this challange.

For example, the acquisition of transient structural data, to $q \approx$1-2Å^{-1}, would enable us to reconstruct transient states that occur during folding using powerful reconstruction programs, such as those designed by Svergun. Time resolved wide angle scattering (TRWAXS) has the potential to report subtle structural changes that are invisible to traditional R_g analysis but are critical to understanding biologically active structures. Given the advances in modeling, this is a promising new direction for following the conformational dynamics of biological molecules in solution.

Numerical estimates. For time resolved SAXS we use pink (2% bandwidth) undulator radiation. From experience at APS 8ID, the unfocused pink beam is about a factor of 10 brighter than what is useful (we attenuate). The beam on the sample is on order 5 μm vertical (normal to the flow stream) and 10 μmm horizontal (partially setting time resolution); the maximum useful intensity is limited by formation of bubbles in the flow channel. The pink beam contains about 10^8 p/s/μm^2 at 7.5 keV, so the useful flux for our typical flow cell experiment is $\sim 5 \times 10^8$ p/s (after attenuation).

For TRWAXS, the bandwidth from a Ge(111) monochromator (3×10^{-4}) is more appropriate.

At APS, on the same sample, but without attenuation, the flux is $\sim 7.5 \times 10^7$ p/s. By comparison at CESR-X, a C-type beamline with two 2.65m (22 mm period) IDs phased to act as one 5.3 m ID should deliver $\sim 3.5 \times 10^9$ p/s at 50 meters (without focusing) using the same monochromator and sample geometry. The superior raw monochromatic flux of CESR-X would enable increased time resolution (by increasing flow speed) or increased signal to noise by more closely matching vertical beam size to the width of the (very narrow) ribbon where mixing occurs.

7.7 Scientific Impact

It has by no means been the objective of this write-up to detail in a comprehensive manner all the possible applications enabled by CESR-X. Other areas where CESR-X is poised to make significant impact include (but are not limited to): macromolecule crystallography, nanomaterial characterization, capillary and other X-ray optics, and phase contrast imaging. In fact, given the history of innovation and productivity at CHESS with the 2nd generation light source, it suffices to say that CESR-X is strategically placed on Cornell campus to capitalize on both CHESS ingenuity, the academic vigor and infrustructure of the University.

8 Near Term Tasks

We have presented an initial study for CESR-X upgrade and made a case for the timeliness of such an upgrade. There are a number of short term tasks that will have to be adressed by the laboratory staff in the nearest future.

Accelerator physics and technology areas will include: Touschek lifetime, injection rate, diagnostics and tuning algorithms, influence of insertion devices on beam, bunch length control, BPMs and orbit feedback. Additionally, we plan to address the eventual upgrade paths, fast timing developments, few picosecond bunch ring operation, "bunch slicing", subpicosecond operation, and ultimately handling of fs ERL-produced bunches.

There is a substantial enineering and planning work ahead: such as minimization of the vacuum chamber bore, design of the vacuum system through reduced-bore quads, magnet modifications, costing, and development of the work breakdown structure.

Finally, there is a slew of activities having to do with the new X-ray beamlines themselves, design of insertion devices and high heat load optics, understanding and planning for the civil construction implications for the Wilson lab. This can only be accomplished as a joint, both CHESS and CESR, laboratory activity.

References

[1] Wang and Zhao, *High Pressure in Carbon Nanotubes,* Science, **312**, 1149, 2006

[2] From SPECTRA8 calculations for full power in radiation cone

[3] Qun Shen, *X-Ray Flux, Brilliance, and Coherence, of the Proposed Cornell Energy Recovery Synchrotron Source,* CHESS Technical Memo 01-002, 2001

[4] G. Kellstrom, Nova Acta Soc. Sci. Upsala, **8**, 5-66, 1932

[5] R. Talman, *Accelerator X-Ray Sources,* Wiley-VCH Verlag, Weinheim, 2006, Eq. (11.39)

[6] J. Als-Nielsen and D. McMorrow, *Elements of Modern X-Ray Physics,* John Wiley, 2001

[7] S. Techart, et al. *Picosecond X-Ray Diffraction Probed Transient Structural Changes in Organic Solids,* Phys. Rev. Lett., **86**, 2030, 2001

[8] Joel Brock, private communication. Pulse durations in the 100 femtosecond range produced by laser "slicing" will permit this class of experiment.

[9] R. Talman, *A Quick, Cheap, Rearranged-CESR Route to the Brilliance Frontier,* CBN 07-10, 2007

[10] R. Talman, *Accelerator X-Ray Sources,* Wiley-VCH Verlag, Weinheim, 2006

[11] Design Report, Cornell Electron Storage Ring, April, 1977

[12] K. Soong, *Lattice Design for a Very High Brightness X-Ray Storage Ring,*, CBN 07-12, 2007

[13] G. Ingold et al., *FEMTO: A Sub-ps Tunable Hard X-ray Undulator Source for Laser/X-ray Pump-Probe Experiments at the SLS,* Synch. Rad. News, **20**, No. 5, 2007

[14] H. Wiedemann, *Brightness of Synchrotron Radiation from Electron Storage Rings,* Nucl. Instr. Meth., 172 (1980)

[15] available at http://femm.forster-miller.net

[16] Mark Palmer, private communication and M. Palmer, et al. *Design, Fabrication and Characterization of a Large-Aperture Quadrupole Magnet for CESR-C,* CBN 05-12, 2005

[17] "The SPEAR-3 Closeout Report", 2004

[18] P. Den Hartog et al., *Dual Canted Undulators at the Advanced Photon Source,* 2003 Particle Accelerator Conference, page 833

[19] For example see work by W. E. Bailly (Columbia U) and co-workers; `http://magnet.ap.columbia.edu`, and PRL **98** (11) 117601, 2007

[20] A. Ruoff et al. Rev. Sci. Instr. **61**, 3830, 1990, and Rev. Sci. Instr. **63**, 4342, 1992

[21] A standard method in "all optical" measurements: phase of probe pulse is adjusted to sample at a specified point in the oscillatory response.

[22] P. Debye, Ann. Phys., **46**, 809, 1915

[23] T. Egami and S. Billinge, *Underneath the Bragg Peaks, Structural Analysis of Complex Materials,* Pergamon Materials Series, Elsevier, 2003

[24] S. Billinge and M. Kanatzidis. *Beyond Crystallography: the Study of Disorder, Nanochrystallinity, and Chrystallographically Challenged Materials with Pair Distribution Functions,* Chem. Comm., 749, 2004

[25] Petkov et al., Phys. Rev. Lett., **83**, 4089

[26] Y. Xiao, et al, *An X-Ray Nanodiffraction Technique for Structural Characterization of Individual Nanomaterials,* J. Synchrotron. Rad., **12**, 124, 2005

[27] H. Grote and F. Iselin, *The MAD Program (Methodical Accelerator Design) Version 8.19, User's Reference Manual,* CERN/SL/90-13 (AP), 1996